Published in final edited form as:

Cell Rep. 2021 June 08; 35(10): 109212. doi:10.1016/j.celrep.2021.109212.

High-fat diet-activated fatty acid oxidation mediates intestinal stemness and tumorigenicity

Miyeko D. Mana[1,2,*], **Amanda M. Hussey**[1], **Constantine N. Tzouanas**[3,4,5,6], **Shinya Imada**[1], **Yesenia Barrera Millan**[2], **Dorukhan Bahceci**[1,14], **Dominic R. Saiz**[2], **Anna T. Webb**[1,15], **Caroline A. Lewis**[7], **Peter Carmeliet**[8,9,10], **Maria M. Mihaylova**[11,12], **Alex K. Shalek**[3,4,5,6], **Ömer H. Yilmaz**[1,4,13,16,*]

[1]Department of Biology, The David H. Koch Institute for Integrative Cancer Research at MIT, Massachusetts Institute of Technology, Cambridge, MA 02139, USA

[2]School of Life Sciences, Arizona State University, Tempe, AZ 85287, USA

[3]Ragon Institute of MGH, MIT, and Harvard, Cambridge, MA 02139, USA

[4]Broad Institute of MIT and Harvard, Cambridge, MA 02142, USA

[5]Institute for Medical Engineering & Science, Department of Chemistry, and Koch Institute for Integrative Cancer Research, Massachusetts Institute of Technology, Cambridge MA 02139, USA

[6]Program in Health Sciences & Technology, Harvard Medical School, Boston, MA 02115, USA

[7]Whitehead Institute for Biomedical Research, Cambridge, MA 02142, USA

[8]Laboratory of Angiogenesis and Vascular Metabolism, Center for Cancer Biology, VIB, and Department of Oncology, Leuven Cancer Institute, KU Leuven, Leuven 3000, Belgium

[9]State Key Laboratory of Ophthalmology, Zhongshan Ophthalmic Center, Sun Yat-Sen University, Guangzhou 510060, Guangdong, P.R. China

[10]Department of Biomedicine, Aarhus University, Aarhus 8000, Denmark

[11]Department of Biological Chemistry and Pharmacology, Ohio State University, Columbus, OH 43210, USA

[12]The Ohio State University Comprehensive Cancer Center, Columbus, OH 43210, USA

[13]Department of Pathology, Massachusetts General Hospital and Harvard Medical School, Boston, MA 02114, USA

[*]Correspondence: miyeko.mana@asu.edu (M.D.M.), ohyilmaz@mit.edu (Ö.H.Y.).

AUTHOR CONTRIBUTIONS

M.D.M. and A.M.H. designed, conducted, and interpreted the experiments with support from Ö.H.Y. C.N.T. and A.K.S. conducted and analyzed scRNA-seq. S.I., D.B., Y.B.M., D.R.S., and A.T.W. provided experimental support. C.A.L. analyzed and interpreted the LC-MS data. P.C. and M.M.M. provided mouse strains. M.M.M. contributed to interpretation of the *Ppar* experiments. M.D.M., A.M.H., and Ö.H.Y. wrote the manuscript, and all authors edited the manuscript.

SUPPLEMENTAL INFORMATION

Supplemental information can be found online at https://doi.org/10.1016/j.celrep.2021.109212.

DECLARATION OF INTERESTS

The authors declare no competing interests.

[14]Present address: Department of Pathology, University of California, San Francisco, San Francisco, CA 94143, USA

[15]Present address: Department of Cell and Molecular Biology, Karolinska Institutet, Stockholm, Sweden

[16]Lead contact

SUMMARY

Obesity is an established risk factor for cancer in many tissues. In the mammalian intestine, a pro-obesity high-fat diet (HFD) promotes regeneration and tumorigenesis by enhancing intestinal stem cell (ISC) numbers, proliferation, and function. Although PPAR (peroxisome proliferator-activated receptor) nuclear receptor activity has been proposed to facilitate these effects, their exact role is unclear. Here we find that, in loss-of-function *in vivo* models, PPARα and PPARδ contribute to the HFD response in ISCs. Mechanistically, both PPARs do so by robustly inducing a downstream fatty acid oxidation (FAO) metabolic program. Pharmacologic and genetic disruption of CPT1A (the rate-controlling enzyme of mitochondrial FAO) blunts the HFD phenotype in ISCs. Furthermore, inhibition of CPT1A dampens the pro-tumorigenic consequences of a HFD on early tumor incidence and progression. These findings demonstrate that inhibition of a HFD-activated FAO program creates a therapeutic opportunity to counter the effects of a HFD on ISCs and intestinal tumorigenesis.

Graphical abstract

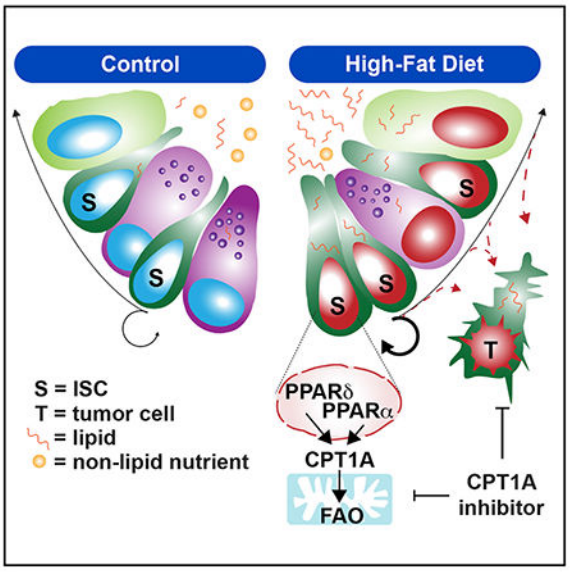

In brief

Mana et al. demonstrate that a high-fat diet enhances intestinal stemness and tumorigenicity through a PPAR-FAO program. The PPAR family members δ and α redundantly activate a robust FAO program in stem cells where loss or inhibition of CPT1a (the mitochondrial long-chain FAO rate-controlling step) dampens these HFD effects.

INTRODUCTION

Obesity increases the incidence and mortality of many types of cancer, including those of the intestine (Calle and Kaaks, 2004; Lauby-Secretan et al., 2016). Many factors contribute to how obesity elevates colon cancer risk, including changes in systemic growth factors (Andres et al., 2015; Calle and Kaaks, 2004; Mah et al., 2014), visceral adipose tissue (Huffman et al., 2013), the microbiome (Arkan, 2017; Schulz et al., 2014), bile acids (Fu et al., 2019), inflammation (Grivennikov et al., 2012; Poullis et al., 2004), and dietary constituents (Beyaz et al., 2016; Wang et al., 2018; Yang et al., 2005). Diet in particular stands out as an important environmental and lifestyle factor that directly affects intestinal regeneration and tumorigenesis. For example, we and others have shown that constituents of a Western diet (a diet rich in fat and sugar), such as excess fatty acids (Beyaz et al., 2016; Fu et al., 2019; Park et al., 2016), cholesterol (Wang et al., 2016), high-fructose corn syrup (Goncalves et al., 2019), as well as low vitamin D (Peregrina et al., 2015), contribute to intestinal tumor formation through distinct mechanisms. These different dietary interventions mimic aspects of obesogenic diets in humans and increase tumorigenesis. Understanding precisely how each one does so will provide novel insights into how early cancers form or whether metabolic programs imposed by such diets can be exploited therapeutically.

The intestinal epithelial lining is at the frontline of digestion and absorption and is maintained by actively cycling *Lgr5*$^{+}$ intestinal stem cells (ISCs) that are located at the base of intestinal crypts (Barker et al., 2007) and respond to dietary cues (Alonso and Yilmaz, 2018). These *Lgr5*$^{+}$ ISCs reside in a supportive microenvironment, or niche, comprised of small-intestine Paneth cells (Rodríguez-Colman et al., 2017; Sato et al., 2011), colonic deep secretory cells (Sasaki et al., 2016), stromal immune cells (Biton et al., 2018; Lindemans et al., 2015), and mesenchymal cell types (Degirmenci et al., 2018; McCarthy et al., 2020; Shoshkes-Carmel et al., 2018) that provide instructive signals to stem cells. *Lgr5*$^{+}$ ISCs can respond directly or indirectly to diet through their niche. For example, low-calorie diets activate *Lgr5*$^{+}$ ISCs indirectly via the Paneth cell niche (Igarashi and Guarente, 2016; Yilmaz et al., 2012) and directly by engaging a fatty acid oxidation (FAO) program in *Lgr5*$^{+}$ ISCs (Mihaylova et al., 2018). Ketone bodies, which are terminally oxidized products of FAO, mediate some of the direct effects of diet on ISCs by modulating Notch signaling (Cheng et al., 2019). Thus, diverse strategies exist that enable ISCs to coordinate tissue adaptation with dietary cues.

We and others recently proposed that a pro-obesity high-fat diet (HFD) increases intestinal tumorigenesis by inducing many direct changes in *Lgr5*$^{+}$ ISCs, which are the cells of origin for a majority of early dysplasias in the intestine (Barker et al., 2009; Beyaz et al., 2016; Mah et al., 2014). These HFD-mediated alterations in *Lgr5*$^{+}$ ISCs include expansion of their numbers per crypt, higher proliferation, and enhanced regenerative capacity (Beyaz et al., 2016), and this expansion in the pool of proliferative ISCs might contribute to how a HFD elevates cancer risk. We also demonstrated mechanistically that ISCs from HFD-fed mice and organoids exposed exogenously to dietary lipids engage a peroxisome proliferator-activated receptor (PPAR) transcriptional program and that pharmacologic activation of PPARδ with a high-affinity agonist, GW501516 (GW), was sufficient to recapitulate many

aspects of the HFD ISC phenotype, including augmentation of their tumorigenic potential, thereby linking lipid sensing with stemness and tumorigenicity.

PPARs include a family of lipid-activated nuclear receptors (α, δ, and γ) that form obligate heterodimers with the retinoid X receptor (RXR) (Barak et al., 2002; Krey et al., 1993) and, upon ligand stimulation, which includes dietary fats or their derivatives, drive PPAR-specific transcriptional programs (Barish et al., 2006; Ordentlich et al., 2001). Although our initial study (Beyaz et al., 2016) implicated PPARδ signaling in the HFD intestinal phenotype, the *in vivo* necessity of this program remains unsettled. Furthermore, GW has been reported to be a highly selective agonist for PPARδ, but it is plausible that some of its effects occur through activation of other PPAR family members, requiring *in vivo* loss-of-function experiments to clarify the role of PPARs in the HFD intestine. Finally, PPAR family members have overlapping downstream targets (Forman et al., 1997) and, because of functional redundancy of PPARs, it may be possible to identify and target common downstream effectors that become active in the HFD state for therapeutic purposes.

Intestinal adaptation to a HFD may involve multiple downstream roles of PPAR targets. PPARδ, for instance, plays critical roles in intestinal physiology through regulation of lipid absorption, cholesterol trafficking, and enteroendocrine cell function (Daoudi et al., 2011; Oliver et al., 2001; Poirier et al., 2001). In particular, CPT1A-mediated FAO is a common metabolic process strongly activated by the PPAR family members δ and δ (Mascaró et al., 1998). We observed previously that HFD-derived or GW agonist-treated ISCs and progenitors significantly upregulate genes involved in FAO (Beyaz et al., 2016); however, the functional role of FAO in mediating aspects of the HFD or PPAR response in ISCs and tumors that arise from them is unclear. Here we investigate the necessity of *Ppard* and *Ppara* and their FAO metabolic program as drivers of ISC adaptation to a HFD and whether HFD-imposed FAO is a therapeutic vulnerability for the genesis and progression of early intestinal adenomas.

RESULTS

PPARδ and PPARα contribute redundantly to the effects of a HFD in ISCs

To determine the *in vivo* role of *Ppard* in driving ISC adaptation in response to HFD feeding (the macronutrient content is listed in Figure S1A), we generated a *Ppard*$^{fl/fl}$*; Vil-CreER* strain to selectively delete *Ppard* in a tamoxifen-inducible manner in the intestinal epithelium. At 6–7 weeks of age, *Ppard*$^{fl/fl}$*; Vil-CreER* (*Ppard*-iKO) or *Ppard*$^{fl/fl}$ (wild type [WT]) were treated with tamoxifen, and then cohorts were placed on a control diet or HFD (Figures 1A and S1A). After 24–28 weeks, small intestinal crypts from control-fed *Ppard*-WT and -iKO mice were equally clonogenic in an organoid assay for stemness. However, although HFD crypts were more clonogenic than controls, loss of *Ppard* led to a modest decrease (Figure 1B), indicating that PPARδ contributes partially to HFD-stimulated crypt clonogenicity (Figures 1B and 1C; Beyaz et al., 2016). Separately, we used an alternate deletion strategy where *Ppard* was ablated after the establishment of HFD-induced obesity (Figures S1B and S1C). Loss of *Ppard* in this model had no effect on crypt clonogenicity (Figures S1B and S1C). In contrast to the mild effects of PPARδ on HFD ISC activity in organoid assays, long-term *Ppard* loss prevented expansion and proliferation of OLFM4^{+}

and *Lgr5*-EGFP^{+} ISCs in the HFD state and partially restored Paneth cell numbers (Figures S1D–S1G). Given that some features of the HFD state, like ISC numbers, but not elevated function, are counteracted by *Ppard* loss, these data raise the possibility that functional redundancy among PPAR family members in the HFD state may compensate for loss of *Ppard*.

To explore this possibility in more detail, we assessed how expression of *Ppara* and *Pparg* and their target genes changed with loss of *Ppard* in control and HFD intestines (Figure 1D). By qRT-PCR and RNAscope *in situ* hybridization (ISH), deficiency of *Ppard* led to altered expression of *Ppara* and *Pparg* transcripts and PPAR targets such as *Pdk4*, *Cpt1a*, *Mgll*, *Fabp1*, and *Hmgcs2* in HFD crypts compared with WT controls (Figures 1D, S1H, and S1I). We generated *Ppard*$^{fl/fl}$*; Vil-CreER; Lgr5-eGFP* mice, a model that disrupts *Ppard* in a tamoxifen-inducible and intestine-specific manner and allows flow cytometry isolation of *Lgr5*-EGFP^{hi} ISCs or *Lgr5*-EGFP^{low} progenitors, to further probe how PPAR targets change in sorted control and HFD ISCs or progenitors at the protein level after *Ppard* loss. *Ppard* loss did not affect the protein abundance of CPT1A and HMGCS2 in *Lgr5*-EGFP^{+} ISCs and progenitors (Figure 1E), consistent with the notion that other PPARs may be involved in the HFD ISC response. However, FABP1 mRNA and protein expression differed with *Ppard* loss on the HFD (Figures 1D and 1E); FABP1 protein levels, but not mRNA levels, respond to the HFD in a PPARδ-dependent manner, illustrating that mRNA levels need not dictate protein expression and that FABP1 likely undergoes post-transcriptional regulation to account for these differences.

Next we turned our attention to *Ppara*, which, like *Ppard*, plays a critical role in regulating FAO metabolism (Evans et al., 2004). *In vivo* activation of PPARα for 30 days with an agonist, WY-14643 (Kliewer et al., 1994), not only increased expression of PPAR targets but also enhanced OLFM4^{+} and *Lgr5*-EGFP^{+} ISC numbers and crypt organoid clonogenicity, demonstrating that activated PPARα and PPARδ have similar effects on stem cell activity (Figures 1F and S1J–S1L; Beyaz et al., 2016). To test whether *Ppara* compensated for *Ppard* loss in HFD organoids, we treated control and HFD crypts from WT and *Ppard*-iKO mice with a PPARα inhibitor, GW6471 (Figure S1M; Xu et al., 2002). Notably, treatment with the PPARα inhibitor reduced the clonogenicity of HFD *Ppard*-iKO crypts to control levels and had no effect in the control or HFD WT groups (Figure S1M), indicating that PPARα and PPARδ are required for elevated HFD crypt function in the organoid assay. To further characterize the *in vivo* necessity of *Ppara*, we used a previously generated whole-body null mouse model (Lee et al., 1995) that was fed a control diet or a HFD. *Ppara* loss by itself mitigated the HFD-enhancing effects on ISC numbers and crypt clonogenicity (Figures S1N and S1P) but had no effect on their proliferation (Figure S1O). These findings indicate that PPARδ and PPARα have distinctive and redundant roles in supporting intestinal progenitor cell adaptation to a HFD.

To further examine the effects of *Ppard* and *Ppara* loss *in vivo,* we generated compound mice with inducible deletion of intestinal *Ppard* on a *Ppara* whole-body null background (Lee et al., 1995), *Ppard*$^{fl/fl}$*; Ppara*^{null}*; Vil-CreER* (*Ppard/a*-iKO). We then treated WT and compound mutant (*Ppard/a*-iKO) mice with tamoxifen and established cohorts on a control diet or HFD for 24 weeks prior to analysis (Figures 1G and S1A). As observed with the

Ppara mutant and inhibitor studies, *in vivo* loss of *Ppara* and *Ppard* was necessary to prevent increased crypt clonogenicity (Figure 1K) in acute and chronic loss of intestinal *Ppard* in the *Ppara*-null background. In addition, loss of both PPARs blocked expansion of OLFM4^{+} ISCs *in vivo* (Figures 1H and 1I) as well as induction of the PPAR program in *Lgr5*-EGFP^{hi} ISCs and GFP^{low} progenitors, as seen in immunoblots or transcriptional analysis (Figures 1J, S1T, and S1U). ISC proliferation and Paneth cell numbers were also maintained at control WT levels (Figures S1R and S1S). Utilizing *Ppard*$^{fl/fl}$*; Ppara*^{null}*; Lgr5-CreER; Rosa-LSL-LacZ*$^{fl/fl}$ engineered mice to further test the *in vivo* role of *Ppars* on ISCs, we found that loss of *Ppard* and *Ppara* reduced lineage output specifically in the HFD state (Figures S1V and S1W). Last, compound *Ppard* and *Ppara* loss prevented HFD crypt survival and regeneration after a lethal dose of radiation (Figures S1X and S1Y). Our data illustrate that PPARδ and PPARα overlappingly contribute to the HFD response in intestinal stem and progenitor cells.

In our prior study (Beyaz et al., 2016), we had functionally validated that the PPARδ agonist GW was sufficient to emulate many of the effects of the HFD on ISCs. However, given that PPARδ and PPARα play redundant roles in the HFD ISC response, some effects of GW may act through stimulation of PPARα. To address this scenario, we treated WT, *Ppard*-iKO, *Ppara*-null, and *Ppard/a*-iKO organoids with GW for 8 days and performed RNA sequencing to probe the specificity of GW in engaging a PPAR or FAO transcriptional program (Beyaz et al., 2021). Although GW treatment in WT and *Ppara*-null mice (genotypes with intact PPARδ) led to strong gene set enrichment for signatures related to PPAR signaling pathways and lipid/fatty acid metabolism, *Ppard* deficiency reduced, but did not entirely eliminate, these signatures as double *Ppard/a*-deficiency did, nor did *Ppard* deficiency block the increase in PPAR transcriptional targets (Figures S1Z–S1BB). These findings indicate that at least some of GW's activity involves PPARα.

FAO drives the ISC HFD and PPAR response

Upon ligand stimulation, PPARδ and PPARα induce a robust transcriptional program that drives fatty acid uptake and breakdown through FAO (Finck et al., 2002; Kersten et al., 1999; Wang et al., 2003). To understand the extent to which HFD activates a FAO transcriptional program (Figure 2A), we performed single-cell RNA sequencing on control and HFD crypts extracted from three regions of the intestine: the proximal and distal small intestine and the colon (Figures S2A–S2C). We confirmed that PPAR target and FAO genes are highly enriched throughout the intestine in these HFD ISC populations compared with controls (Figures 2B and S2D). In addition, through liquid chromatography-mass spectrometry (LC-MS), we found that metabolites such as acetylcarnitine and β-hydroxybutyrate (BOHB), known products of FAO, were more abundant in HFD crypts (Figures 2C and 2D). We then exposed HFD and control crypts to tritium-labeled palmitate to measure production of tritiated H_2O, which serves as a proxy for FAO rates in cells (Manning et al., 1990; Nieman et al., 2011), and observed that HFD crypts were nearly 2-fold more capable of FAO than controls (Figure 2E). Given that HFD primes for FAO metabolism, we wanted to find out how the cellular capacity of the crypt to use other fuel sources is affected using isotope-labeled substrates for glucose and glutamine. We incubated control and HFD crypts with U^{13}C-glucose or U^{13}C-glutamine and then measured formation of labeled downstream metabolites. Interestingly, with U^{13}C-glucose, we observed that HFD

crypt cells incorporated fewer carbons into lactate and citrate than controls, supporting the notion that glucose metabolism is diminished in HFD ISCs and progenitors (Figures S2E–S2I). However, neither diet showed a preference for $U^{13}C$-glutamine as an alternate fuel source (Figures S2J–S2L). These data demonstrate that HFD crypts increase FAO and concomitantly decrease glucose oxidation.

Given that CPT1A, the rate-controlling enzyme in FAO, is highly expressed in HFD ISCs by gene expression (Figure 2B), mRNA ISH (Figure 2F), and protein immunoblots (Figures 1E and 1J), we wanted to find out whether FAO inhibition would attenuate the HFD-induced increase in organoid formation. We incubated crypts from control and HFD-fed mice in organoid assays with increasing concentrations of etomoxir, an irreversible inhibitor of CPT1A, to ascertain the role of FAO as an effector of the HFD response (Figures 2H and 2I). Although etomoxir had no effect on the ability of control crypts to form organoids, treatment with etomoxir dampened HFD crypt clonogenicity in a dose-dependent manner (Figures 2G and 2H). Similarly, PPARδ (GW) or PPARα (WY-14643, WY) agonist treatment in the organoid assay boosted FAO rates and sensitivity to etomoxir-mediated FAO inhibition (Figures S2M and S2N), highlighting the functional importance of FAO as a downstream target of the HFD-PPAR axis. Addition of octanoate, an 8-carbon fatty acid that bypasses CPT1A-mediated entry into mitochondria, counteracted the inhibitory effects of etomoxir on HFD crypt clonogenicity and *Lgr5*-eGFP^{+} organoids (Figures 2I–2K). Although exogenous octanoate had no additional effect on HFD crypt clonogenicity, likely because these crypts are already in a state of elevated FAO, stimulation of control crypt organoid formation with exogenous octanoate was observed (Figures 2I–2K and S2O–S2Q). In contrast, lactate or pyruvate, glycolytic metabolites that feed into the TCA cycle to undergo oxidation, fail to alleviate the effects of FAO inhibition on HFD crypt clonogenicity (Figure 2I).

CPT1A-mediated FAO promotes HFD ISC stemness

Next we sought to investigate the *in vivo* necessity of FAO metabolism in control and HFD ISCs using tamoxifen-inducible and intestine-specific *Cpt1a*$^{fl/fl}$*; Vil-CreER; Lgr5-eGFP* mice (Figure 3A). Consistent with our prior study (Mihaylova et al., 2018), acute deletion of *Cpt1a* for 4 weeks in control intestines had no effect on OLFM4^{+} or *Lgr5*-EGFP^{+} ISC numbers (Beyaz et al., 2021; Figures 3B–3E) or on stem and progenitor cell proliferation, as assessed with a 4-h pulse of bromodeoxyuridine (BrdU^{+}) (Figures 3D and S3A). However, *Cpt1a* deletion in HFD intestines restored ISC numbers (Figures 3B and 3D) and proliferation to control levels (Figures 3D and S3A) and blocked the organoid-enhancing effects of a HFD on crypts (Figure 3F) and sorted *>Lgr5*-EGFP^{hi} ISCs (Figure 3G). Using a *Lgr5-CreER; Rosa-LSL-LacZ*$^{fl/fl}$ lineage tracer, loss of *Cpt1a* reduced β-galactosidase (β-gal) lineage tracing from control and HFD stem cells but with a greater reduction in HFD crypts (Figures S1V and S1W). In addition, long-term *Cpt1a* loss (Figures S3E and S3F) prior to initiation of a HFD also blunted the regenerative effects of a HFD on crypts in the organoid assay (Figure S3K) and following injury from ionizing radiation (Figures S3L and S3M), indicating that HFD-induced FAO in ISCs and progenitors promotes recovery after damage. Acute (1 month) and long-term (6–7 months) *Cpt1a* loss had mild effects on intestinal differentiation, as assessed by quantification of Lysozyme^{+} Paneth cell numbers, ChromograninA^{+} (CgA^{+}) neuroendocrine cell, or Alcian blue^{+} goblet cell numbers (Figures

S3B–S3D and S3H–S3J). Although a HFD decreases Paneth cell numbers, as we noted previously (Beyaz et al., 2016), it does so in a CPT1A-dependent manner because long-term *Cpt1a* loss rescues this decline (Figure S3H). Finally, *Cpt1a* loss prevented expansion and proliferation of stem/progenitor cells in the HFD crypt (Figures S3A and S3G).

As expected, loss of *Cpt1a* in HFD crypts led to many metabolic changes compared with controls. FAO from surplus free fatty acids (FFAs) provided by the HFD, for example, generates acetyl-coenzyme A (CoA), which can feed into ketogenesis and the TCA cycle (Figure 2A). Loss of *Cpt1a* led to decreased FAO in HFD crypts (Figure S3Q) and resulted in significant reductions in levels of FAO-associated metabolites, such as acetylcarnitine and BOHB (Figures 3H and S3N). Moreover, the abundance of the TCA intermediate citrate was lower in HFD *Cpt1a*-iKO crypts compared with controls, presumably due to loss of FAO-derived acetyl-CoA (Figure S3P), whereas pyruvate levels increased concomitantly, representing an adaptation to decreased flux through the TCA cycle (Figure S3O). Notably, although loss of *Cpt1a* dramatically diminished crypt BOHB levels, it also led to a compensatory boost in HMGCS2 protein, independent of diet, in sorted EpCAM^{+} intestinal epithelial cells, ISCs, and progenitors (Figure 3I). A possible explanation for this observation is that FAO disruption through *Cpt1a* deletion reduces acetyl-CoA feeding into ketogenesis, which accounts for the diminishment of BOHB, whereas FFAs continue to stimulate sensors such as PPARδ and PPARα to transcribe genes involved in FAO and lipid metabolism (Figures S3R and S3S), including HMGCS2 (a known PPAR target) (Figure 3I). This upregulation of HMGCS2, after FAO disruption, permits crypt BOHB levels to remain stable on a control diet and to maintain at least basal levels in HFD crypts (Figure S3N). This finding is consistent with our recent studies implicating BOHB as a key metabolite that regulates intestinal stemness and dietary responses (Cheng et al., 2019; Gebert et al., 2020). Overall, these findings support the notion that a shift toward FAO in a HFD accounts for many of the metabolic and functional changes that occur in ISCs.

Intestinal tumors that arise on a HFD are sensitive to FAO inhibition

A pro-obesity HFD induces many changes in intestinal stem and progenitor cells, such as expanding their numbers, proliferation, and function by engaging a robust PPAR-FAO program. It is possible, for example, that tumors arising from ISCs in a HFD state retain a similar sensitivity to FAO inhibition as their non-tumor counterparts, raising the question of whether a HFD creates a therapeutic opportunity to exploit FAO dependencies in these tumors. To assess this possibility, we utilized conditional *Apc*$^{fl/fl}$*; Lgr5-eGFP-IRES-CreER* (*Apc*-iKO) mice where tamoxifen administration leads to loss of both copies of *Apc* in *Lgr5*$^{+}$ ISCs and rapid tumor formation, permitting study of early intestinal tumor formation in response to diet (Figure 4A; Barker et al., 2009; Beyaz et al., 2016; DeClercq et al., 2015).

We placed *Apc*-iKO mice on a control or HFD for 1 month, and then induced *Apc* excision with a single tamoxifen injection. As expected, HFD feeding dramatically accelerated mortality in this model compared with the control condition (Figure 4B; Beyaz et al., 2016; Park et al., 2016). Many lines of evidence indicate that HFD-stimulated FAO mediates this accelerated tumorigenesis. First, *Apc*-null tumors and *Lgr5*-EGFP^{+} tumor cells from HFD

mice demonstrate heightened expression of *Cpt1a* and *Hmgcs2* by ISH and immunoblots relative to controls (Figures S4A and S4B). Second, HFD tumors, as determined 4 days after *Apc* loss in *Apc*$^{fl/fl}$*; Vil-CreER* mice (Figures S4B and S4C) and as predicted from the expression of *Cpt1a* and *Hmgcs2*, have higher levels of FAO-associated metabolites like acetylcarnitine and BOHB (Figure 4C). Third, loss of *Cpt1a* in mice on a HFD significantly reduced the number and size of spontaneous *Apc*-null adenomas formed in a loss-of-heterozygosity model compared with *Cpt1a*-WT control counterparts (Figures S4K and S4L). Fourth, genetic disruption of *Cpt1a* in *Cpt1a*$^{fl/fl}$*; Apc*$^{fl/fl}$*; Lgr5-eGFP-IRES-CreER* mice, where a single tamoxifen dose concomitantly deletes *Cpt1a* and *Apc* in *Lgr5*$^{+}$ ISCs, dramatically dampened the numbers and area of β-catenin-positive tumors 20 days after tamoxifen administration in mice on an HFD for 7 weeks, whereas there was no effect on control diet tumors (Figures 4D–4F and S4D). Furthermore, HFD tumors were enriched for greater numbers of *Cpt1a*-competent escapers than what was observed in the controls, highlighting an important role of FAO in HFD tumor maintenance (Figures S4E and S4F). Last, to address how *Cpt1a* dampens HFD-mediated tumorigenesis, we administered three doses of tamoxifen over 8 days to *Apc*-iKO mice to maximize *Cpt1a* deletion. Acute *Cpt1a* loss reduced HFD-stimulated proliferation, as measured by Ki67, which also corresponded to decreased DNA damage and apoptosis, as assessed by γH2AX and C-Casp3 immunofluorescence, respectively (Figures S4G–S4J). Although these data highlight that a HFD boosts adenomatous proliferation in a CPT1A-dependent manner, it is unclear whether the decrease in DNA damage or apoptosis with *Cpt1a* loss in an HFD stems indirectly from reduced proliferation or tumor size or directly from *Cpt1a* loss itself.

Although co-deletion of *Cpt1a* and *Apc* in *Lgr5*$^{+}$ HFD ISCs reduced tumor initiation and burden when FAO was disrupted genetically at the beginning of tumor formation, we turned our focus to investigating whether FAO inhibition in established adenomas would also have growth-retarding effects in a HFD. To test this scenario, we induced *Apc* loss in *Apc*-iKO mice, maintained cohorts on a control diet or HFD for 20 days, and then mice were injected with daily doses of etomoxir starting on day 11 (Figure 4G). Analogous experiments were also performed with PPARδ and PPARα agonists (GW and WY, respectively) to understand the role of PPARs in this process (Figure 4G). While HFD and PPARα and PPARδ agonist treatments boosted tumor numbers (Figure S4N), etomoxir had no effect on adenoma multiplicity because tumors were initiated prior to etomoxir treatment. Etomoxir, however, did blunt the growth-enhancing effects of HFD and GW, but not WY, on adenoma size (Figures 4H, 4I, S4M, and S4N), indicating that the HFD and these agonists mediate some of their tumorigenic effects via FAO.

To test the effect of decreased FAO in HFD-induced adenomas in the colon (Figure 2B), we generated *Apc*$^{fl/fl}$*; Cpt1a*$^{fl/fl}$*; Vil-CreER* and, similarly, *Apc*$^{fl/fl}$*; Ppard*$^{fl/fl}$*; Ppara*^{null}*; Vil-CreER* mice and injected 4-OH tamoxifen using an endoscopy-guided approach to induce adenoma formation specifically in the distal colon (Figures 4J and 4K). *Ppard*; *Ppara* loss in colonic adenomas significantly diminished tumor size in a HFD-dependent manner, analogous to their roles in actuating the HFD response in intestinal stem and progenitor cells (Figure 4K). *Cpt1a* loss decreased tumor size irrespective of diet, but there was a much larger reduction on the HFD, consistent with the notion that HFD tumors are more sensitive to *Cpt1a* inhibition (Figure 4K). Furthermore, *Cpt1a*-null tumor cells, which were strongly

selected against (Figure S4O), were less proliferative than their *Cpt1a* competent counterparts (Figure S4P). These data demonstrate that a HFD drives intestinal tumorigenesis in part by shifting tumor cell metabolism toward FAO metabolism and creates a therapeutic opportunity for tumor prevention or treatment by targeting the FAO pathway in the HFD state.

DISCUSSION

Here we propose that a HFD enhances intestinal stemness and tumorigenicity by engaging a PPAR-FAO program. Although we have suggested previously that PPARδ is the main PPAR family member that underlies the HFD ISC response, we now modify this view because PPARα also contributes to ISC regulation in a pro-obesity high-lipid environment. Compensation of PPARδ loss by PPARα is compatible with an earlier study that proposed that PPARδ inhibits PPARα activity, underscoring the complexity of PPAR biology in physiological states such as HFD-induced obesity (Shi et al., 2002). Because it can be therapeutically challenging to inhibit this redundancy in HFD ISCs, both of these PPARs converge on and elicit a robust FAO program where pharmacologic or genetic disruption of CPT1A-mediated FAO blunts the HFD-enhancing effects on ISCs or tumors that arise from them (Figure 4L). Disruption of this PPAR-FAO axis has minimal effects on baseline intestinal homeostasis (Figures 1 and S1), in contrast to other regulators of lipid metabolism, such as PRDM16 and HNF4α/γ (Chen et al., 2020; Stine et al., 2019). One possible explanation for this discrepancy is that PPARs, by sensing lipid availability, permit ISCs to adapt to diverse dietary states, especially ketotic states induced by an HFD, fasting, and ketogenic diets. PPARs, in the setting of a HFD, augment FAO in ISCs as a response to surfeit dietary lipids, but their genetic loss does not compromise basal FAO or ISC function (Figures 1J and 1K). Different from PPARs, PRDM16 and HNF4α/γ play an obligatory role in regulating basal FAO because their loss significantly hampers intestinal stemness in a FAO-dependent fashion (Chen et al., 2020; Stine et al., 2019).

Another important implication of our work is in regard to the role of FAO in stem cell biology and intestinal tumorigenesis (Shapira and Christofk, 2020). A PPARδ-FAO axis is necessary for maintaining the HSC pool (Ito et al., 2012), and FAO governs neural progenitor quiescence (Knobloch et al., 2017). It has also been proposed that limiting mitochondrial pyruvate metabolism by deletion of mitochondrial pyruvate carrier 1 (*Mpc1*) in the intestine and hair follicles promotes stemness (Flores et al., 2017; Schell et al., 2017). Subsequently, Bensard et al. (2020) have shown that loss of *Mpc1* leads to a pro-tumorigenic phenotype (Bensard et al., 2020). A shared feature of *Mpc1* loss and HFD-activated PPAR signaling is that both interventions restrict the participation of pyruvate in the TCA cycle and compensate by boosting FAO. With this metabolic shift, *Mpc1* loss, like a HFD, enhances the contribution of fatty-acid-derived acetyl-CoA to the TCA cycle in *ex vivo* cultures (Schell et al., 2017). We have shown here and previously (Mihaylova et al., 2018) that FAO inhibition blunts the ISC-enhancing effects of a HFD and PPAR agonists, but deciphering how much of the ISC and pro-tumorigenic phenotype associated with *Mpc1* deletion occurs though FAO versus other sequelae of altered carbohydrate metabolism will be an important future endeavor.

An intriguing similarity of fasting (Mihaylova et al., 2018) and a HFD is that both interventions augment ISC function through engagement of a PPAR-FAO program. However, fasting and HFD are believed to have very different effects on health and cancer incidence. Although both diets strongly induce FAO for utilization of circulating FFAs as an energy source, the extent of fatty acid saturation of the mitochondrial FAO machinery is quite different between these two diets, which may ultimately affect tumor formation. In a HFD, ISCs are exposed to surplus amounts of FFAs, whereas in fasting, ISCs need to scavenge energy from a limited quantity of FFAs to satisfy their energy needs. In a HFD, excessive amounts of FFAs likely overwhelm the mitochondria and lead to generation of reactive lipids and reactive oxygen species that have a cumulative deleterious effect over time, which does not occur with fasting, where FFAs are much less abundant.

A remaining question is which factor(s) downstream of FAO contribute to the ISC-enhancing effects of FAO. We recently discovered that the ketone body BOHB plays a part in regulating ISC homeostasis and their dietary responses. BOHB is a terminally oxidized lipid byproduct of FAO that has energetic and signaling properties (Newman and Verdin, 2017; Puchalska and Crawford, 2017) and further serves as a class 1 histone deacetylase inhibitor to reinforce the NOTCH program in ISCs (Cheng et al., 2019). BOHB levels increase dramatically in ISCs from ketotic states induced by HFDs (Figure 2D), fasting (Mihaylova et al., 2018), and ketogenic diets (KDs) (Cheng et al., 2019), and all of these diets are associated with improved ISC function. Future studies will need to delineate the precise roles of mitochondrial activity and ketone bodies, such as the energetic and NOTCH signaling properties of BOHB, in accounting for the similarities and differences between HFD, fasting, and KD regimens on intestinal stemness and tumorigenicity.

From a therapeutic perspective, the precise role of *Ppard* in intestinal tumorigenesis has been a matter of debate, in part because of the commonly used agonist GW and different genetic models utilized to model *Ppard* loss, the latter of which has been reviewed previously (Beyaz and Yilmaz, 2016; Wagner and Wagner, 2020). For example, GW treatment accelerates intestinal tumorigenesis in an Apc^{min} model (Gupta et al., 2004) and promotes metastasis in orthotopic colon cancer cell line models (Wang et al., 2019). Based on our initial work showing that GW recapitulates the HFD ISC response (Beyaz et al., 2016), we suggested that PPARδ signaling coupled a HFD with enhanced intestinal stemness. However, as we find here, GW also has PPARα-stimulating properties (Figures S1Z–S1BB), raising the possibility that at least some of its effects on ISCs and early tumors are through PPARα. A previous study demonstrated that PPARα in loss-of-function and agonist treatment experiments enhances and attenuates DSS/chemically-induced AOM intestinal tumorigenesis, respectively, which is different from what we observe in the HFD *Apc* loss-of-function model (Luo et al., 2019). One possibility is that DSS/AOM promotes tumorigenesis by not only transforming intestinal epithelial cells but also by inciting inflammation and that PPARα has a protective role in inflammation-driven tumorigenesis, a process relevant to inflammatory bowel disease. Future lines of investigation will need to decipher how PPARs mediate intestinal tumorigenesis in inflammation and obesity and in tumors with complex genetics beyond that achieved with DSS/AOM or *Apc* loss.

Importantly, induction of FAO is a shared downstream and targetable feature of the HFD-induced PPARδ/α program that can be exploited to ameliorate the stemness and cancer consequences of this obesity model. Wang et al. (2019) found that a HFD-activated *Nanog* program facilitates colon cancer metastasis in a PPARδ-dependent manner (Wang et al., 2019). It is possible, for example, that FAO actuates some of the downstream effects of *Nanog* and offers a therapeutic metabolic target for colon cancer progression and metastasis in this dietary model. Additionally, epithelial FAO may have non-cell-autonomous effects that influence the tumor microenvironment in a HFD state, leading to disease progression (Ringel et al., 2020). Finally, as interest in exploiting diet-induced metabolic vulnerabilities grows and as our understanding of pathways that govern these approaches expands (Kanarek et al., 2020; Lien and Vander Heiden, 2019; Tajan and Vousden, 2020), exploration of whether FAO inhibition can be leveraged therapeutically in HFD or PPAR agonist-stimulated tumors will be compelling to pursue.

STAR★METHODS

RESOURCE AVAILABILITY

Lead contact—Further information and requests for resources and reagents should be directed to and will be fulfilled by Ömer H. Yilmaz (ohyilmaz@mit.edu, (Ö.H.Y.)).

Materials availability—All in-house generated mouse strains generated for this study are available from the Lead Contacts with a completed Materials Transfer Agreement.

Data and code availability—RNA-seq and scRNA-seq data generated for this study are available at Gene Expression Omnibus (GEO) with the following accession numbers GSE151047, GSE164832.

EXPERIMENTAL MODEL AND SUBJECT DETAILS

Mice were under the husbandry care of the Department of Comparative Medicine in the Koch Institute for Integrative Cancer Research. All procedures were conducted in accordance with the American Association for Accreditation of Laboratory Animal Care and approved by MIT's Committee on Animal Care. The following strains were obtained from the Jackson Laboratory: Lgr5-eGFP-IRES-CreERT2 (strain name: B6.120P2-Lgr5tm1(cre/ERT2)Cle/J, stock number 008875), Rosa26-LSL-lacZ (strain name: B6.129S4-Gt(ROSA)26Sortm1Sor/J, stock number 003474), $Ppard^{fl/fl}$ (B6.129S4-$Ppard^{tm1Rev}$/J, stock number 005897), and $Ppara^{-/-}$ (129S4/SvJae-$Ppara^{tm1Gonz}$/J, stock number 003580). $Cpt1a^{fl/fl}$ mouse strain has been previously described (Schoors et al., 2015). Villin-CreERT2 mouse strain was a gift from Sylvie Robine and was previously described (el Marjou et al., 2004). $Apc^{fl/fl(exon\ 14)}$ ($Apc^{fl/fl}$) has been previously described (Colnot et al., 2004). The following strains were bred in-house: 1) $Ppard^{fl/fl}$; $Ppara^{-/-}$; Villin-CreERT2; Lgr5-eEGFP-IRES-CreERT2, 2) $Ppard^{fl/fl}$; $Ppara^{-/-}$; Villin-CreERT2, 3) $Cpt1a^{fl/fl}$; Villin-CreERT2; Lgr5-eGFP-IRES-CreERT2, 4) $Cpt1a^{fl/fl}$; $Apc^{fl/fl}$; Lgr5-eGFP-IRES-CreERT2, Rosa26-LSL-$LacZ^{fl/fl}$,5) $Apc^{fl/fl}$; Lgr5-eGFP-IRES-CreERT2; Rosa26-LSL-$LacZ^{fl/fl}$,6) $Ppard^{fl/fl}$; $Ppara^{-/-}$; $Apc^{fl/fl}$; Villin-CreERT2, 7) $Cpt1a^{fl/fl}$; $Apc^{fl/fl}$; Villin-CreERT2, 8) $Apc^{fl/fl}$; Villin-CreERT2, 9) $Ppard^{fl/fl}$; $Ppara^{-/-}$; Lgr 5-eEGFP-IRES-CreERT2; Rosa26-LSL-$LacZ^{fl/fl}$, 10)

Cpt1a$^{fl/fl}$; Lgr5-eEGFP-IRES-CreERT2; Rosa26-LSL- LacZ$^{fl/fl}$, 11) Ppard$^{fl/fl}$; Villin-CreERT2, 12) Ppard$^{fl/fl}$; Villin-CreERT2; Lgr5^{+}-eEGFP-IRES-CreERT2,13) Ppara$^{-/-}$; Lgr5-eEGFP-IRES-CreERT2, 14) Apc$^{fl/+}$; Lgr5-eGFP-IRES-CreERT2; Rosa-LSL-LacZ$^{fl/fl}$,15) Apc$^{fl/+}$; Cpt1a$^{fl/fl}$; Lgr5-eGFP-IRES-CreERT2; Rosa-LSL-LacZ$^{fl/fl}$. Long-term high-fat diet (containing 60% kcal from fats (Research Diets D12492)) was provided to male and female mice at the age of 8-12 weeks for 6 to 8 months. Control mice were provided either standard chow (LabDiet, 5P76) or a purified Control diet (10 kcal% fats, matching sucrose, Research Diets, D12450J). All mice were sex and aged matched, and provided food *ad libitum.* PPARδ agonist GW501516 (Sigma Aldrich, SML1491) was reconstituted in DMSO at 20 mg/ml and diluted 1:10 in a solution of 5% PEG400 (Sigma Aldrich, P4338), 5% Tween80 (Sigma Aldrich, P4780), 90% water for daily intraperitoneal injection for 30 days. PPARα agonist WY-14643 (Sigma Aldrich, C7801) was reconstituted in water at 20 mg/ml and diluted in the same injection solution described above. Floxed alleles were excised following intraperitoneal injection of tamoxifen suspended in 1 part 100% ethanol: 9 parts sunflower seed oil (Spectrum S1929) at a concentration of 10 mg/ml and dosed at 100mg/kg. Mice harboring conditional alleles were administered tamoxifen three times within one week unless otherwise specified. BrdU (Sigma Aldrich, 19-160) was prepared at 10 mg/ml in PBS and injected at 100 mg/kg 4 hours prior to harvesting tissue with the exception of induced colon tumors in which the time interval between injection and collection was 1 hour.

METHOD DETAILS

Crypt isolation and culture—Small intestines were removed, flushed with PBS$^{-/-}$(no calcium, no magnesium), opened laterally, gently wiped to remove mucus layer and cut into ~10cm sections. Intestine pieces were rinsed 3 times and incubated at 4°C in PBS$^{-/-}$ + 10 mM EDTA for 45 min. Crypts were then mechanically separated from the connective tissue by shaking, and filtered through 70μm mesh into a 50 mL conical tube to remove villi and tissue fragments. Isolated crypts were counted and embedded in 3.5:6.5 media: Matrigel (Corning 356231 growth factor reduced) mixture at 5-10 crypts per μl and cultured in a crypt culture medium modified from Sato et al. (2009). Unless otherwise described, crypts were grown in Advanced DMEM (GIBCO, 12491015) supplemented with EGF 40 ng/ml (Peprotech, 315-09), Noggin 200 ng/ml (Peprotech 250-38), R-Spondin 500 ng/ml (Peprotech, 315-32), *N*-acetyl-L-cysteine 1 μM (Sigma Aldrich, A9165), B27 1x (Life Technologies, 17504044), Chir99021 1 μM (LC Laboratories, C-6556), Y-27632 dihydrochloride monohydrate 10 μM (Sigma Aldrich, Y0503). Intestinal crypts were plated in 10 (5 μl) droplets of Matrigel and placed on flat bottomed 48 (96) well plates (Olympus 25-108 (48) 25-109 (96)) and allowed to solidify for 15 min in a 37°C incubator. 250/150 μL of crypt medium was added to each well and maintained at 37°C in a humidified incubator at 5% CO_2. Crypt medium was changed every three days. Clonogenicity (colony-forming assay) was assessed on day 3 or as specified. Etomoxir in PBS (0 –100 μM, Sigma Aldrich, E1905) was added to the cultures 12 hours after plating, media was exchanged on day 3 and clonogenicity assessed on day 5. PPARα antagonist GW6471 (Tocris, 4618) was reconstituted in DMSO and provided to culture at 1 μM. For the carbon substrate supplementation experiments, basal media was RPMI (GIBCO, no glucose, 11879020) supplemented with 5mM glucose (Sigma Aldrich, D7021), the same growth additives as mentioned above for crypt culture, and one of the following carbon sources: sodium

octanoate (1 mM, Sigma Aldrich, C5048 sodium pyruvate (500 μM, Sigma Aldrich, P8574), or sodium lactate (5 mM, Sigma Aldrich, L7022) were added to respective wells of culture with or without Etomoxir (37.5 μM) in a 96 well plate for 4 days. Organoid images were acquired on Nikon Ti Eclipse epifluorescence microscope equipped with LCD light source (lumencor light engine® SOLA, SM 5-LCR-SA) and sCMOS camera (Andor Zyla 4.2 cMOS).

Flow isolated Lgr5-eGFP^{hi} ISCs were centrifuged at 250 g for 5 minutes, re-suspended in the appropriate volume of crypt medium and seeded onto 15 μL of Matrigel (Corning 356231 growth factor reduced) containing 1 μM JAG-1 protein (Anaspc, AS-61298) in a flat bottom 48-well plate (Olympus, 25-108).

qRT-PCR and *in situ* hybridization—Approximately 10,000 crypts were resuspended in 400 μL of TRI Reagent (Sigma Aldrich, 93289) and total RNA was isolated according to the manufacturer's instructions. RNA was converted to cDNA using qScript cDNA SuperMix (Quantabio, 95048-100). qRT-PCR reaction was performed using diluted cDNA (1:20) 3 wells with SYBR green fast mix (Quantabio, PerfeCTa, 95072-012) on a Roche lightcycler (Roche, LightCycler 480 II). Primers used are described on the Key resources table.

Single molecule *in situ* hybridization was performed using Advanced Cell Diagnostics RNAscope 2.5 HD Detection Kit. The *in situ* hybridization probes used in this study are as follows: Mm-Cpt1a (Ref 443071), Mm-Pparα (Ref 454051).

Immunoblotting—The following antibodies were used: mouse monoclonal anti-Cpt1a (1:500(sorted), (1:1000crypt lysates), Abcam ab128568), rabbit monoclonal anti-HMGCS2 (1:500(sorted), 1:1000(crypt lysates), Abcam, ab137043), rabbit monoclonal anti-FABP1 (1:1000, CST, 13368), monoclonal rabbit anti-PDK4 (1:1000, Abcam, ab214938), rabbit monoclonal γ-tubulin (1:1000, Sigma-Aldrich, T5198) and monoclonal anti-rabbit total H3 (1:3000, CST 4449S).

Lgr5-eGFP^{hi} ISCs, Lgr5-eGFP^{low} progenitors, or EpCAM+ cells were sorted directly into 6X Laemmli sample buffer (Alfa Aesar, J61337) and boiled for 5 minutes. Either 10,000 cells were loaded per sorted sample or 10ug of crypt lysates were loaded per sample onto a 4%–12% gradient gel, transferred on to PVDF membrane (Immobilon-P transfer, Millipore, ipvh00010), and analyzed using IgG-HRP antibodies (1:3000, CST, 7076, 7074) and Advansta WesternBright Sirus ECL detection kit (K12043D20).

Immunohistochemistry (IHC) and immunofluorescence (IF)—Tissues were fixed in 10% formalin, paraffin embedded and sectioned in 4-5micron sections as previously described (Yilmaz et al., 2012). Antigen retrieval was performed using Borg Decloaker RTU solution (Biocare Medical, BD1000G1) and a pressurized Decloaking Chamber (Biocare Medical, NxGen). Antibodies and respective dilutions used for immunohistochemistry are as follows: rabbit monoclonal anti-OLFM4 (1:10,000, CST, 39141), rabbit monoclonal anti-GFP (1:1000, CST, 2956S), mouse monoclonal anti-β-catenin (1:200, BD Biosciences, 610164), rat anti-BrdU (1:2000, Abcam 6326), rabbit polyclonal anti-lysozyme (1:2000, Thermo RB-372-A1), rabbit polyclonal anti-ChromograninA (1:4000, Abcam 15160), and

rabbit polyclonal anti-KI67 (1:4000, Abcam, ab15580). Biotin-conjugated secondary donkey anti-mouse, anti-rabbit, or anti-rat antibodies were used (1:500, Jackson ImmunoResearch). Vectastain Elite ABC immunoperoxidase detection kit (Vector Laboratories, PK6100) was followed by Signalstain® DAB substrate kit for visualization (CST, 8049S). All antibody dilutions were performed in Signalstain® Antibody Diluent (CST, 8112L). The following primary antibodies were used for immunofluorescence: rabbit monoclonal anti β-catenin (1:500, Abcam, 32572), mouse monoclonal anti-CPT1a (1:250, Abcam, ab128568), rat Anti-BrdU (1:2000, Abcam ab6326), or rabbit cleaved caspase 3 (Asp 175) (5A1E) (1:1000, CST, 9664S). Alexa Fluor secondary antibodies, anti-mouse 488, anti-rabbit 568, and anti-rat 594, were used for visualization. Tissue was mounted using Invitrogen Prolong Gold mounting medium containing DAPI. Images were acquired using a 20x objective (Nikon Plan Apo) using a Nikon Eclipse 90i upright microscope equipped with a Hamamatsu Orca-ER CCD camera, and APC line 1200 light source.

Isolation of ISCs and flow cytometry—Following crypt isolation, the crypt suspensions were pelleted (100 g, 5 min, 4°C) and supernatant was discarded. Crypts were resuspended in TrypLE (GIBCO, no phenol red, 12604039) and dissociated into individual cells by warming crypts in water bath at 32°C for 60 s. Dissociated single cells were treated with the following antibody cocktail for flow cytometry analysis: CD45-PE (eBioscience, 12-0451-83), CD31-PE (Biolegend, 102514), Ter-119PE (Biolegend, 116208), CD24-Pacific Blue (Biolegend, 101820), CD117-APC/Cy7 (Biolegend, 105826), and EpCAM-APC (eBioscience, 17-5791-82). 7AAD (Invitrogen, A1310) was used a viability dye to exclude dead cells from the analysis. ISCs were isolated as Lrg5-eGFP^{hi}EpCAM $^{+}$CD24$^{low/-}$CD31^{-}Ter119^{-}CD45^{-}7AAD^{-}. eGFP^{low} progenitors were isolated as Lrg5-eGFP^{low}EpCAM^{+}CD24$^{low/-}$CD31^{-}Ter119^{-}CD45^{-}7AAD^{-}. Cells were sorted using a BD FACS II SORP cell sorter.

Loss of heterozygosity—Apc$^{fl/+}$; Lgr5-eEGFP-IRES-CreERT2; ± Cpt1a$^{fl/fl}$ mice were injected with tamoxifen (100mg/kg) 3 times and placed on either High Fat or Control diet for 6 months. Upon tissue collection, small intestines were flushed, cut in half, fixed in 10% formalin, paraffin embedded, and sectioned into 4-5 micron sections. Sections were subsequently stained for β-catenin (BD Pharmagen) to enumerate adenomatous legions and CPT1a (Abcam) to identify the contribution of CPT1a null clones in the adenomas.

Lineage tracing analysis—The protocol for lineage tracing has been previously published (Barker and Clevers, 2010). In brief, mice harboring Lgr5-eEGFP-IRES-CreERT2; Rosa-LSL-LacZ were injected with tamoxifen (100mg/kg) 72 hours prior to sacrifice. The small intestine was removed and 5 cm of jejunum and ileum were fixed in glutaraldehyde fixative solution for 2 hours. The tissue was then washed with 1x PBS + 0.02% NP-40 and placed in β-galactosidase (lacZ) substrate solution for 5 hours at 37°C and then 14 hours at 4°C. Samples were washed with 1x PBS, placed in 10% formalin solution, paraffin embedded using a short xylene cycle, and sectioned into 4-5 micron sections. Section slides were deparaffinized, rehydrated, and counterstained with 0.1% neutral red. Blue LacZ+ CBC+ crypts were identified and the length from the base of the crypt to the highest LacZ+ cell along the migratory trajectory was measured.

RNA-seq data processing and differential expression analysis—Single-end RNA-seq reads were aligned to a transcriptome derived from the mm10 primary assembly with an ensembl v.88 annotation using STAR version 2.5.3a (Dobin et al., 2013) and gene expression was summarized using RSEM version 1.3.0 (Li and Dewey, 2011), samtools version 1.3 (Li et al., 2009). Differential expression analysis was done with R version 3.4.4 using DESeq2_1.18.1 (Anders and Huber, 2010) and normal log fold change shrinkage. The resulting data were parsed and assembled using Tibco Spotfire Analyst version 7.11.1.

3′ DGE FASTQ sequencing reads were collapsed to one representative read per unique molecular identifier using a custom python script. Gene expression was quantified using salmon (version 1.1.0) (Patro et al., 2017) using a transcriptome prepared from the mouse mm10 primary genome assembly using the ensembl version 98 annotation. The resulting counts were summarized to the gene level using R (version 3.6.2) running tximport (version 1.12.3) (Soneson et al., 2015) and counts per million (cpm) were calculated using utilities implement in edgeR (version 3.26.8) (Chen et al., 2016). The cpm values with a +1 offset were transformed to log2 space for visualization. Differential expression for treatments within cell lines and between untreated cell lines was done using DESeq2 (version 1.24.0) (Love et al., 2014) and apeglm log fold change shrinkage. Data assembly and visualization was done using Tibco Spotfire Analyst (version 7.11.1). Pre-ranked Gene Set Enrichment Analysis (version 4.0.3) (Subramanian et al., 2005) was run using DESeq2 Wald statistic as a ranking metric and gene set collections from msigDB (version 7.0) (Liberzon et al., 2015).

scRNA-seq Seq-Well library preparation—Seq-Well with second-strand synthesis was performed as previously described (Aicher et al., 2019; Gierahn et al., 2017; Hughes et al., 2020). Briefly, dissociated cells from the proximal small intestine, distal small intestine, or colon of mice were diluted to a concentration of 15,000 cells in 200 μL, then added to a functionalized PDMS microarray pre-loaded with mRNA capture beads (Chem-Genes). After four washes with PBS and one wash with RPMI, the array was sealed with a plasma-functionalized polycarbonate membrane (pore size 0.01 μm). To seal the membrane to the array surface, the array was placed at 37°C for 40 minutes, followed by lysis in guanidium thiocyanate (Sigma), 1mM EDTA, 1% beta-mercaptoethanol and 0.05% sarkosyl (Sigma) for 20 minutes at room temperature. Afterward, lysis buffer was exchanged via gentle rocking in hybridization buffer to facilitate mRNA hybridization to the capture bead, containing 2M NaCl (Fisher Scientific) with 8% (v/v) polyethylene glycol (PEG, Sigma) for 40 minutes at room temperature. Beads were collected in a wash buffer containing 2M NaCl, 3mM $MgCl_2$, 20mM Tris-HCl, and 8% (v/v) PEG, followed by reverse transcription with Maxima H Minus Reverse Transcriptase (Fisher Scientific) for 30 minutes at room temperature and overnight at 52°C, all with end-over-end rotation. Exonuclease I digestion (New England BioLabs) was carried out according to manufacturer's instructions, followed by bead washes in TE with 0.01% Tween-20 (TE-TW, Fisher Scientific) and TE with 0.5% SDS (TE-SDS, Sigma). For second-strand synthesis, beads were denatured using 5 minutes of end-over-end rotation in 0.1 M NaOH. Beads were then washed with TE-TW and TE, followed by 60 minutes at 37°C in second-strand synthesis reaction mixture (Hughes et al., 2020). KAPA HiFi Hotstart Readymix and ISPCR primer were used to carry out PCR (95°C for 3 minutes; 4 cycles of 98°C for 20 s, 65°C for 45 s, 72°C for 3 minutes; 12 cycles of

98°C for 20 s, 67°C for 20 s, 72°C for 3 minutes; 5-minute extension at 72°C). cDNA was purified using an AMPure XP SPRI bead cleanup, with an initial 0.6X volume ratio, followed by a 0.8x volume ratio. 900 pg of purified cDNA library per sample was used as the input to Nextera XT DNA Sample Preparation kit. Sequencing libraries were purified through the same SPRI bead cleanup ratios (i.e., 0.6X and 0.8X volume ratios) and confirmed to have a length distribution with an average of 500-750 base pairs (Agilent hsD1000 Screen Tape System). Samples were sequenced through Illumina paired-end sequencing on a NovaSeq 6000. Read 1 began from a custom read 1 primer for 20 bases (12bp cell barcode, 8bp UMI), and read 2 contained 50bp of transcript information.

Seq-Well data alignment, filtering, and analysis—Version 2.1.0 of the Drop-seq pipeline was used to align sequencing reads to a custom reference genome that consisted of *eGFP* added to the standard mm10 reference genome. Demultiplexed FASTQs were aligned to the custom reference genome through STAR and the Drop-seq pipeline, implemented on the Broad Institute's Terra cloud computing platform. Through alignment, reads were grouped based on cell barcode and collapsed if UMIs were separated by a Hamming distance of 1, forming digital gene expression matrices for each sample.

DGEs were pre-processed to remove cells with fewer than 500 genes detected (likely corresponding to detection of ambient RNA or low-quality cells), more than 75,000 UMIs (likely corresponding to doublets), or more than 35% of UMIs corresponding to mitochondrial genes (likely indicating low-quality cells with ruptured membranes). Data was then analyzed using Seurat in R (Stuart et al., 2019), with normalization implemented via SCTransform's regularized negative binomial regression. Cells were designated as stem cells if *Lgr5* or *eGFP* were detected, as either natural or transgenic markers of stem cell identities, respectively. Notably, across the relevant sample metadata used in these comparisons (i.e., diet condition and stem cell identity), quality metrics did not exhibit large differences, supporting that differences in gene expression are not artifacts of sample/sequencing quality (Figure S2A–B). For downstream visualization and clustering, principal component analysis was performed on the highly variable genes returned from SCTransform, with a choice of 21 principal components made by examining the elbow plot of variance explained by each principal component (results robust against alternate choices of QC and visualization parameters). UMAP visualization was implemented using the "uwot" R package on the 21 principal components.

Module scores in stem cell populations were calculated with Seurat's "AddModuleScore" function, with the PPARδ module comprised of *Hmgcs2, Angptl4, Pdk4, Acsl3, Me1, Aco1, Reg3g*, and *Plin2*, genes designated as PPARδ targets from Figure S1BB. The stem module is based on top stem cell markers from Smillie et al. (2019). Importantly, *Lgr5* was one of the top stem cell markers (Smillie et al., 2019); we removed it prior to scoring our dataset, given that it was used as a marker for calling stem cells in our study and could provide an upward bias when comparing $Lgr5^{+}$ to $Lgr5^{-}$ populations. Nonetheless, populations called as stem cells in our study exhibited increased stemness scores compared to remainder cells, as expected. Significance of differences in the distribution of gene expression/module score between high fat and control diet stem cells was assessed using the non-parametric Mann-Whitney test (implemented as "wilcox.test" function in R, with "alternative" set to "greater"

to evaluate the hypothesis that expression of PPARδ target genes involved in fatty acid oxidation is increased in high fat diet stem cells), and p values were corrected for multiple hypothesis testing using the Benjamini-Hochberg (implemented with “p.adjust” function in R, with “method” set to “Hochberg”).

Metabolomics, U^{13}C-glucose and U^{13}C-glutamine tracing, and LC/MS methods —Crypts were harvested in cold PBS+EDTA, pelleted, washed once with saline and resuspended in LC/MS grade 80% methanol containing internal standard solutions (909 nM each of 17 isotopically labeled amino acids, Cambridge Isotope Laboratories, MSK-A2-1.2). Samples were vortexed for 10 min at 4°C, centrifuged for 10 min at 4°C, and separated from the pellet. Samples were then dried in a vacuum dryer, resuspended in 100 μl of LC/MS grade water, and analyzed by LC/MS as described (Birsoy et al., 2015). For labeling experiments, crypts were isolated from mice on either Control or HFD in cold PBS+EDTA, rinsed with saline, and subsequently incubated in RPMI (GIBCO, no glucose, 11879020) containing above mentioned crypt medium components plus 11mM glucose, 2mM glutamine and 30 μM Palmitate. Crypts were incubated for 60 min at 37°C, 5% CO_2. For glucose labeling experiments, isolated crypts were incubated with 11 mM U^{13}C-glucose (Cambridge Isotopes, CLM-1396-PK) in supplemented RPMI for 60 min at 37°C, 5% CO_2. For glutamine labeling experiments, isolated crypts were incubated with 2 mM U^{13}C-glutamine (Cambridge Isotopes, CLM-1822H-PK) in supplemented RPMI for 60 min at 37°C, 5% CO_2. The polar metabolites were extracted by the addition of LC/MS grade methanol, water and chloroform. The mixture was vortexed for 10 min at 4°C and then centrifuged for 10 min at 4°C. The aqueous fraction was carefully removed from the chloroform fraction and both the polar and the non-polar fraction were transferred to clean microfuge tubes and dried using a vacuum centrifuge. The polar fraction was analyzed as described above (Birsoy et al., 2015). Stable isotope tracing data corrected for natural abundance using an in-house script as discussed in Buescher et al. (2015).

For LC-MS, 2 μl of each sample was injected onto a ZIC-pHILIC 2.1 × 150 mm (5 μm particle size) column (MilliporeSigma). Buffer A was 20 mM ammonium carbonate, 0.1% ammonium hydroxide; buffer B was acetonitrile. The chromatographic gradient was run at a flow rate of 0.150 ml/min as follows: 0-20 min.: linear gradient from 80% to 20% B, 20-20.5 min.: linear gradient from 20% to 80% B; 20.5-28 min.: hold at 80% B. The mass spectrometer, QExactive orbitrap, was operated in full-scan, polarity switching mode with the spray voltage to 3.0 kV, the heated capillary was held at 275°C and the HESI probe held at 350°C. The sheath gas flow was set to 40 units, the auxiliary gas flow was set to 15 units, and the sweep gas flow was set to 1 unit. The MS data acquisition was performed in a range of 70-1000 m/z, with the resolution set at 70,000, the AGC target at 10^6 and the maximum injection time at 80 msec. Relative quantitation of polar metabolites was performed with Tracefinder4.1 (Thermo Fisher Scientific) using a 5ppm mass tolerance and referencing an in-house library of chemical standards.

Fatty acid oxidation assay—Isolated crypts (4000, estimated 1 million cells) were plated on a 24 well plate coated with 10% Matrigel (Corning 356231 growth factor reduced) in 400 μL crypt medium (RPMI (GIBCO, no glucose, 11879020) basal medium with 5mM

glucose) and allowed to incubate in a humidified 37°C incubator at 5% CO_2 for 15 min. 10% essentially fatty acid free BSA (Sigma Aldrich, A6003) in PBS was complexed at a volume ratio of 6.7:3 with palmitic acid-[9,10-^{3}H] (Pekin Elmer, NET043001MC) by vortexing for 60 s and was added at a 1:100 ratio to crypt medium. This hot medium was split into half and Etomoxir (75 μM final) was added to inhibit FAO. 100 μl of the hot FFA:PA:medium mixture was added to the incubated crypts, for a total volume of 500 μl, and were incubated for 1 hour, 37°C, 5% CO_2. Samples were removed from the wells and pelleted at 21K *rcf.* for 2:30 min. 400 μL of resulting supernatant was transferred to a filter column (Fisher Scientific, 11-387-50) containing 3 mL of activated Dowex®1X8 resin (Sigma Aldrich, 217425). 2.5 mL of ddH_2O was added to elute ^{3}H-water from the column. 750 μL of eluent was added to 2.5 mL of EcoLume (MP Biomedicals, 882470). Betacounts were measured on a scintillation counter (Beckman Coulter, LS6500).

Irradiation experiments—Mice were challenged by a lethal split dose of irradiation, 7.5Gy x 2 with six hours between exposures. Tissue was collected 72 hours post the last dose. Numbers of surviving crypts were enumerated in the jejunum from Hematoxylin and Eosin stained tissue and identified as robust crypt structures with dense nuclei and presence of Paneth cells.

Orthotopic injection into the colon—Prior to injection, mice 1) Apc$^{fl/fl}$; Villin-CreERT2; 2) Cpt1a$^{fl/fl}$; APC$^{fl/fl}$; Villin-CreERT2, 3) Ppard$^{fl/fl}$; Ppar$^{-/-}$; Apc$^{fl/fl}$; Villin-CreERT2 were placed on either High Fat Diet or matching purified Control Diet for one month. Mice were directly injected in the colon with 50μL of 30 μM (Z)-4-hydroxytamoxifen (resuspended in PBS, single dose) using previously established methods (Roper et al., 2017). Mice remained on their assigned diet for an additional month with optical colonoscopies performed at week 2 and week 4 after injection using a Karl Storz Image1 HD Camera System, Image1 HUB CCU, 175 Xenon Light source, and Richard Wold 1.9mm/9.5Fr Integrated Telescope (Roper et al., 2018). Colonoscopy images were saved for offline analysis. Mice received a 1 hour pulse of BrdU (100mg/kg) prior to tissue collection (1 month). The colon was flushed, lateralized, and imaged using a Nikon SMZ18 stereoscope at 0.75x magnification for gross tumor analysis. Colons were then fixed in 10% formalin, paraffin embedded, and sectioned to the widest point of the individual tumors. Tumor sections were stained with β-catenin (BD Pharmogen) for IHC. Subsequent tumor sections were stained with Cpt1a (Abcam) and BrdU (Abcam) for IF analysis of the tumors.

QUANTIFICATION AND STATISTICAL ANALYSIS

Unless otherwise specified in the figure legends, all experiments reported in this study were repeated at least five independent times. Unless otherwise specified in the main text or figure legends, all sample number (n) represent biological replicates. For murine organoid assays, 2-5 wells per mouse per *ex vivo* treatment were analyzed. All center values shown in graphs refer to the mean. No sample or animals were excluded from analysis and sample size estimates were not used. Animals were randomly assigned to groups. Experiments used roughly equivalent male and female mice to avoid sex bias. Studies were not conducted blind with the exception of all histological analyses. Please note that statistical details are found in the figure legends. All experiments involving mice were carried out with the

approval from the Committee for Animal Care at MIT and under the supervision of the Department of Comparative Medicine at MIT.

Supplementary Material

Refer to Web version on PubMed Central for supplementary material.

ACKNOWLEDGMENTS

We thank the Whitehead Institute Metabolite Profiling Core Facility, the Whitehead Institute Flow Cytometry Core, and the Swanson Biotechnology Center at the Koch Institute, which encompasses the Flow Cytometry, Histology, and Genomics & Bioinformatics Core facilities (NCI P30-CA14051). We thank Charlie Whittaker for analysis and helpful discussions regarding RNA sequencing data. We thank the Department of Comparative Medicine for mouse husbandry support. We thank Sven Holder and members of the Hope Babette Tang (1983) Histology Facility for substantial histology support. We thank Heaji Shin and Chia-Wei Cheng for comments on the manuscript, Kerry Kelley for laboratory management, and Liz Galoyan for administrative assistance. M.D.M. received support from the American Cancer Society (PF-16-202-01-NEC), an MIT/Ludwig Center for Molecular Oncology postdoctoral fellowship in metastasis/cancer research, and an MIT/Koch Institute quinquennial cancer research fellowship and receives current funding from NIH 1K22CA241083-01. C.N.T. is supported by a Fannie and John Hertz Foundation fellowship and a National Science Foundation graduate research fellowship (1122374). P.C. is supported by grants from Methusalem funding (Flemish government), the Fund for Scientific Research-Flanders (FWO-Vlaanderen), and the European Research Council (ERC advanced research grant EU- ERC743074). M.M.M. is supported by NIH R00 AG054760 and the American Federation of Aging Research (AFAR). A.K.S. is supported by the Pew-Stewart Scholars Program for Cancer Research. Ö.H.Y. is supported by R01CA211184, R01CA034992, and U54CA224068; a Pew-Stewart Trust scholar award; the Kathy and Curt Marble cancer research award; a Koch Institute-Dana-Farber/Harvard Cancer Center Bridge Project grant; and AFAR. C.N.T., A.K.S., and Ö.H.Y. receive support from the MIT Stem Cell Initiative through Fondation MIT.

REFERENCES

Aicher TP, Carroll S, Raddi G, Gierahn T, Wadsworth MH, Hughes TK, Love C, and Shalek AK (2019). Seq-Well: A Sample-Efficient, Portable Picowell Platform for Massively Parallel Single-Cell RNA Sequencing. Methods Mol. Biol 1979, 111–132. [PubMed: 31028635]

Alonso S, and Yilmaz ÖH (2018). Nutritional Regulation of Intestinal Stem Cells. Annu. Rev. Nutr 38, 273–301. [PubMed: 29799767]

Anders S, and Huber W (2010). Differential expression analysis for sequence count data. Genome Biol. 11, R106. [PubMed: 20979621]

Andres SF, Santoro MA, Mah AT, Keku JA, Bortvedt AE, Blue RE, and Lund PK (2015). Deletion of intestinal epithelial insulin receptor attenuates high-fat diet-induced elevations in cholesterol and stem, enteroendocrine, and Paneth cell mRNAs. Am. J. Physiol. Gastrointest. Liver Physiol 308, G100–G111. [PubMed: 25394660]

Arkan MC (2017). The intricate connection between diet, microbiota, and cancer: A jigsaw puzzle. Semin. Immunol 32, 35–42. [PubMed: 28870704]

Barak Y, Liao D, He W, Ong ES, Nelson MC, Olefsky JM, Boland R, and Evans RM (2002). Effects of peroxisome proliferator-activated receptor delta on placentation, adiposity, and colorectal cancer. Proc. Natl. Acad. Sci. USA 99, 303–308. [PubMed: 11756685]

Barish GD, Narkar VA, and Evans RM (2006). PPAR delta: a dagger in the heart of the metabolic syndrome. J. Clin. Invest 116, 590–597. [PubMed: 16511591]

Barker N, and Clevers H (2010). Lineage tracing in the intestinal epithelium. Curr. Protoc. Stem Cell Biol Chapter 5, Unit 5A.4.

Barker N, van Es JH, Kuipers J, Kujala P, van den Born M, Cozijnsen M, Haegebarth A, Korving J, Begthel H, Peters PJ, and Clevers H (2007). Identification of stem cells in small intestine and colon by marker gene Lgr5. Nature 449, 1003–1007. [PubMed: 17934449]

Barker N, Ridgway RA, van Es JH, van de Wetering M, Begthel H, van den Born M, Danenberg E, Clarke AR, Sansom OJ, and Clevers H (2009). Crypt stem cells as the cells-of-origin of intestinal cancer. Nature 457, 608–611. [PubMed: 19092804]

Bensard CL, Wisidagama DR, Olson KA, Berg JA, Krah NM, Schell JC, Nowinski SM, Fogarty S, Bott AJ, Wei P, et al. (2020). Regulation of Tumor Initiation by the Mitochondrial Pyruvate Carrier. Cell Metab. 31, 284–300.e7. [PubMed: 31813825]

Beyaz S, and Yilmaz ÖH (2016). Molecular Pathways: Dietary Regulation of Stemness and Tumor Initiation by the PPAR-δ Pathway. Clin. Cancer Res 22, 5636–5641. [PubMed: 27702819]

Beyaz S, Mana MD, Roper J, Kedrin D, Saadatpour A, Hong S-J, Bauer-Rowe KE, Xifaras ME, Akkad A, Arias E, et al. (2016). High-fat diet enhances stemness and tumorigenicity of intestinal progenitors. Nature 531, 53–58. [PubMed: 26935695]

Beyaz S, Mana MD, and Yilmaz ÖH (2021). High-fat diet activates a PPAR-δ program to enhance intestinal stem cell function. Cell Stem Cell 28, 598–599. [PubMed: 33798420]

Birsoy K, Wang T, Chen WW, Freinkman E, Abu-Remaileh M, and Sabatini DM (2015). An Essential Role of the Mitochondrial Electron Transport Chain in Cell Proliferation Is to Enable Aspartate Synthesis. Cell 162,540–551. [PubMed: 26232224]

Biton M, Haber AL, Rogel N, Burgin G, Beyaz S, Schnell A, Ashenberg O, Su C-W, Smillie C, Shekhar K, et al. (2018). T Helper Cell Cytokines Modulate Intestinal Stem Cell Renewal and Differentiation. Cell 175, 1307–1320.e22. [PubMed: 30392957]

Buescher JM, Antoniewicz MR, Boros LG, Burgess SC, Brunengraber H, Clish CB, DeBerardinis RJ, Feron O, Frezza C, Ghesquiere B, et al. (2015). A roadmap for interpreting (13)C metabolite labeling patterns from cells. Curr. Opin. Biotechnol. 34, 189–201. [PubMed: 25731751]

Calle EE, and Kaaks R (2004). Overweight, obesity and cancer: epidemiological evidence and proposed mechanisms. Nat. Rev. Cancer 4, 579–591. [PubMed: 15286738]

Chen Y, Lun ATL, and Smyth GK (2016). From reads to genes to pathways: differential expression analysis of RNA-Seq experiments using Rsubread and the edgeR quasi-likelihood pipeline. F1000Res. 5, 1438. [PubMed: 27508061]

Chen L, Vasoya RP, Toke NH, Parthasarathy A, Luo S, Chiles E, Flores J, Gao N, Bonder EM, Su X, and Verzi MP (2020). HNF4 Regulates Fatty Acid Oxidation and Is Required for Renewal of Intestinal Stem Cells in Mice. Gastroenterology 158, 985–999.e9. [PubMed: 31759926]

Cheng C-W, Biton M, Haber AL, Gunduz N, Eng G, Gaynor LT, Tripathi S, Calibasi-Kocal G, Rickelt S, Butty VL, et al. (2019). Ketone Body Signaling Mediates Intestinal Stem Cell Homeostasis and Adaptation to Diet. Cell 178, 1115–1131.e15. [PubMed: 31442404]

Colnot S, Niwa-Kawakita M, Hamard G, Godard C, Le Plenier S, Houbron C, Romagnolo B, Berrebi D, Giovannini M, and Perret C (2004). Colorectal cancers in a new mouse model of familial adenomatous polyposis: influence of genetic and environmental modifiers. Lab. Invest. 84, 1619–1630. [PubMed: 15502862]

Daoudi M, Hennuyer N, Borland MG, Touche V, Duhem C, Gross B, Caiazzo R, Kerr-Conte J, Pattou F, Peters JM, et al. (2011). PPARβ/δ activation induces enteroendocrine L cell GLP-1 production. Gastroenterology 140, 1564–1574. [PubMed: 21300064]

DeClercq V, McMurray DN, and Chapkin RS (2015). Obesity promotes colonic stem cell expansion during cancer initiation. Cancer Lett. 369, 336–343. [PubMed: 26455770]

Degirmenci B, Valenta T, Dimitrieva S, Hausmann G, and Basler K (2018). GLI1-expressing mesenchymal cells form the essential Wnt-secreting niche for colon stem cells. Nature 558, 449–453. [PubMed: 29875413]

Dobin A, Davis CA, Schlesinger F, Drenkow J, Zaleski C, Jha S, Batut P, Chaisson M, and Gingeras TR (2013). STAR: ultrafast universal RNA-seq aligner. Bioinformatics 29, 15–21. [PubMed: 23104886]

el Marjou F, Janssen K-P, Chang BH-J, Li M, Hindie V, Chan L, Louvard D, Chambon P, Metzger D, and Robine S (2004). Tissue-specific and inducible Cre-mediated recombination in the gut epithelium. Genesis 39, 186–193. [PubMed: 15282745]

Evans RM, Barish GD, and Wang Y-X (2004). PPARs and the complex journey to obesity. Nat. Med. 10, 355–361. [PubMed: 15057233]

Finck BN, Lehman JJ, Leone TC, Welch MJ, Bennett MJ, Kovacs A, Han X, Gross RW, Kozak R, Lopaschuk GD, and Kelly DP (2002). The cardiac phenotype induced by PPARalpha overexpression mimics that caused by diabetes mellitus. J. Clin. Invest. 109, 121–130. [PubMed: 11781357]

Flores A, Schell J, Krall AS, Jelinek D, Miranda M, Grigorian M, Braas D, White AC, Zhou JL, Graham NA, et al. (2017). Lactate dehydrogenase activity drives hair follicle stem cell activation. Nat. Cell Biol. 19, 1017–1026. [PubMed: 28812580]

Forman BM, Chen J, and Evans RM (1997). Hypolipidemic drugs, polyunsaturated fatty acids, and eicosanoids are ligands for peroxisome proliferator-activated receptors alpha and delta. Proc. Natl. Acad. Sci. USA 94, 4312–4317. [PubMed: 9113986]

Fu T, Coulter S, Yoshihara E, Oh TG, Fang S, Cayabyab F, Zhu Q, Zhang T, Leblanc M, Liu S, et al. (2019). FXR Regulates Intestinal Cancer Stem Cell Proliferation. Cell 176, 1098–1112.e18. [PubMed: 30794774]

Gebert N, Cheng C-W, Kirkpatrick JM, Di Fraia D, Yun J, Schädel P, Pace S, Garside GB, Werz O, Rudolph KL, et al. (2020). Region-Specific Proteome Changes of the Intestinal Epithelium during Aging and Dietary Restriction. Cell Rep. 31, 107565. [PubMed: 32348758]

Gierahn TM, Wadsworth MH 2nd, Hughes TK, Bryson BD, Butler A, Satija R, Fortune S, Love JC, and Shalek AK (2017). Seq-Well: portable, low-cost RNA sequencing of single cells at high throughput. Nat. Methods 14, 395–398. [PubMed: 28192419]

Goncalves MD, Lu C, Tutnauer J, Hartman TE, Hwang S-K, Murphy CJ, Pauli C, Morris R, Taylor S, Bosch K, et al. (2019). High-fructose corn syrup enhances intestinal tumor growth in mice. Science 363,1345–1349. [PubMed: 30898933]

Grivennikov SI, Wang K, Mucida D, Stewart CA, Schnabl B, Jauch D, Taniguchi K, Yu G-Y, Osterreicher CH, Hung KE, et al. (2012). Adenoma-linked barrier defects and microbial products drive IL-23/IL-17-mediated tumour growth. Nature 491, 254–258. [PubMed: 23034650]

Gupta RA, Wang D, Katkuri S, Wang H, Dey SK, and DuBois RN (2004). Activation of nuclear hormone receptor peroxisome proliferator-activated receptor-delta accelerates intestinal adenoma growth. Nat. Med. 10, 245–247. [PubMed: 14758356]

Huffman DM, Augenlicht LH, Zhang X, Lofrese JJ, Atzmon G, Chamberland JP, and Mantzoros CS (2013). Abdominal obesity, independent from caloric intake, accounts for the development of intestinal tumors in Apc(1638N/+) female mice. Cancer Prev. Res. (Phila.) 6, 177–187. [PubMed: 23466815]

Hughes TK, Wadsworth MH 2nd, Gierahn TM, Do T, Weiss D, Andrade PR, Ma F, de Andrade Silva BJ, Shao S, Tsoi LC, et al. (2020). Second-Strand Synthesis-Based Massively Parallel scRNA-Seq Reveals Cellular States and Molecular Features of Human Inflammatory Skin Pathologies. Immunity 53, 878–894.e7. [PubMed: 33053333]

Igarashi M, and Guarente L(2016). mTORC1 and SIRT1 Cooperate to Foster Expansion of Gut Adult Stem Cells during Calorie Restriction. Cell 166, 436–450. [PubMed: 27345368]

Ito K, Carracedo A, Weiss D, Arai F, Ala U, Avigan DE, Schafer ZT, Evans RM, Suda T, Lee C-H, and Pandolfi PP (2012). A PML–PPAR-δ pathway for fatty acid oxidation regulates hematopoietic stem cell maintenance. Nat. Med. 18, 1350–1358. [PubMed: 22902876]

Kanarek N, Petrova B, and Sabatini DM (2020). Dietary modifications for enhanced cancer therapy. Nature 579, 507–517. [PubMed: 32214253]

Kersten S, Seydoux J, Peters JM, Gonzalez FJ, Desvergne B, and Wahli W (1999). Peroxisome proliferator-activated receptor α mediates the adaptive response to fasting. J. Clin. Invest. 103, 1489–1498. [PubMed: 10359558]

Kliewer SA, Forman BM, Blumberg B, Ong ES, Borgmeyer U, Mangelsdorf DJ, Umesono K, and Evans RM (1994). Differential expression and activation of a family of murine peroxisome proliferator-activated receptors. Proc. Natl. Acad. Sci. USA 91, 7355–7359. [PubMed: 8041794]

Knobloch M, Pilz G-A, Ghesquière B, Kovacs WJ, Wegleiter T, Moore DL, Hruzova M, Zamboni N, Carmeliet P, and Jessberger S (2017). A Fatty Acid Oxidation-Dependent Metabolic Shift Regulates Adult Neural Stem Cell Activity. Cell Rep. 20, 2144–2155. [PubMed: 28854364]

Krey G, Keller H, Mahfoudi A, Medin J, Ozato K, Dreyer C, and Wahli W (1993). Xenopus peroxisome proliferator activated receptors: genomic organization, response element recognition, heterodimer formation with retinoid X receptor and activation by fatty acids. J. Steroid Biochem. Mol. Biol. 47, 65–73. [PubMed: 8274443]

Lauby-Secretan B, Scoccianti C, Loomis D, Grosse Y, Bianchini F, and Straif K; International Agency for Research on Cancer Handbook Working Group (2016). Body Fatness and Cancer–Viewpoint of the IARC Working Group. N. Engl. J. Med. 375, 794–798. [PubMed: 27557308]

Lee SS, Pineau T, Drago J, Lee EJ, Owens JW, Kroetz DL, Fernandez-Salguero PM, Westphal H, and Gonzalez FJ (1995). Targeted disruption of the alpha isoform of the peroxisome proliferator-activated receptor gene in mice results in abolishment of the pleiotropic effects of peroxisome proliferators. Mol. Cell. Biol. 15, 3012–3022. [PubMed: 7539101]

Li B, and Dewey CN (2011). RSEM: accurate transcript quantification from RNA-Seq data with or without a reference genome. BMC Bioinformatics 12, 323. [PubMed: 21816040]

Li H, Handsaker B, Wysoker A, Fennell T, Ruan J, Homer N, Marth G, Abecasis G, and Durbin R; 1000 Genome Project Data Processing Subgroup (2009). The Sequence Alignment/Map format and SAMtools. Bioinformatics 25, 2078–2079. [PubMed: 19505943]

Liberzon A, Birger C, Thorvaldsdóttir H, Ghandi M, Mesirov JP, and Tamayo P (2015). The Molecular Signatures Database (MSigDB) hallmark gene set collection. Cell Syst. 1, 417–425. [PubMed: 26771021]

Lien EC, and Vander Heiden MG (2019). A framework for examining how diet impacts tumour metabolism. Nat. Rev. Cancer 19, 651–661. [PubMed: 31530936]

Lindemans CA, Calafiore M, Mertelsmann AM, O'Connor MH, Dudakov JA, Jenq RR, Velardi E, Young LF, Smith OM, Lawrence G, et al. (2015). Interleukin-22 promotes intestinal-stem-cell-mediated epithelial regeneration. Nature 528, 560–564. [PubMed: 26649819]

Love MI, Huber W, and Anders S (2014). Moderated estimation of fold change and dispersion for RNA-seq data with DESeq2. Genome Biol. 15, 550. [PubMed: 25516281]

Luo Y, Xie C, Brocker CN, Fan J, Wu X, Feng L, Wang Q, Zhao J, Lu D, Tandon M, et al. (2019). Intestinal PPARα Protects Against Colon Carcinogenesis via Regulation of Methyltransferases DNMT1 and PRMT6. Gastroenterology 157, 744–759.e4. [PubMed: 31154022]

Mah AT, Van Landeghem L, Gavin HE, Magness ST, and Lund PK (2014). Impact of diet-induced obesity on intestinal stem cells: hyperproliferation but impaired intrinsic function that requires insulin/IGF1. Endocrinology 155, 3302–3314. [PubMed: 24914941]

Manning NJ, Olpin SE, Pollitt RJ, and Webley J (1990). A comparison of [9,10-3H]palmitic and [9,10-3H]myristic acids for the detection of defects of fatty acid oxidation in intact cultured fibroblasts. J. Inherit. Metab. Dis. 13, 58–68. [PubMed: 2109149]

Mascaró C,Acosta E, Ortiz JA, Marrero PF, Hegardt FG, and Haro D (1998). Control of human muscle-type carnitine palmitoyltransferase I gene transcription by peroxisome proliferator-activated receptor. J. Biol. Chem. 273, 8560–8563. [PubMed: 9535828]

McCarthy N, Manieri E, Storm EE, Saadatpour A, Luoma AM, Kapoor VN, Madha S, Gaynor LT, Cox C, Keerthivasan S, et al. (2020). Distinct Mesenchymal Cell Populations Generate the Essential Intestinal BMP Signaling Gradient. Cell Stem Cell 26, 391–402.e5. [PubMed: 32084389]

Mihaylova MM, Cheng C-W, Cao AQ, Tripathi S, Mana MD, Bauer-Rowe KE, Abu-Remaileh M, Clavain L, Erdemir A, Lewis CA, et al. (2018). Fasting Activates Fatty Acid Oxidation to Enhance Intestinal Stem Cell Function during Homeostasis and Aging. Cell Stem Cell 22, 769–778.e4. [PubMed: 29727683]

Newman JC, and Verdin E (2017). β-Hydroxybutyrate: A Signaling Metabolite. Annu. Rev. Nutr. 37, 51–76. [PubMed: 28826372]

Nieman KM, Kenny HA, Penicka CV, Ladanyi A, Buell-Gutbrod R, Zillhardt MR, Romero IL, Carey MS, Mills GB, Hotamisligil GS, et al. (2011). Adipocytes promote ovarian cancer metastasis and provide energy for rapid tumor growth. Nat. Med. 17, 1498–1503. [PubMed: 22037646]

Oliver WR Jr., Shenk JL, Snaith MR, Russell CS, Plunket KD, Bodkin NL, Lewis MC, Winegar DA, Sznaidman ML, Lambert MH, et al. (2001). A selective peroxisome proliferator-activated receptor delta agonist promotes reverse cholesterol transport. Proc. Natl. Acad. Sci. USA 98, 5306–5311. [PubMed: 11309497]

Ordentlich P, Downes M, and Evans RM (2001). Corepressors and nuclear hormone receptor function. Curr. Top. Microbiol. Immunol. 254, 101–116. [PubMed: 11190569]

Park M-Y, Kim MY, Seo YR, Kim J-S, and Sung M-K (2016). High-fat Diet Accelerates Intestinal Tumorigenesis Through Disrupting Intestinal Cell Membrane Integrity. J. Cancer Prev. 21, 95–103. [PubMed: 27390738]

Patro R, Duggal G, Love MI, Irizarry RA, and Kingsford C (2017). Salmon provides fast and bias-aware quantification of transcript expression. Nat. Methods 14, 417–419. [PubMed: 28263959]

Peregrina K, Houston M, Daroqui C, Dhima E, Sellers RS, and Augenlicht LH (2015). Vitamin D is a determinant of mouse intestinal Lgr5 stem cell functions. Carcinogenesis 36, 25–31. [PubMed: 25344836]

Poirier H, Niot I, Monnot MC, Braissant O, Meunier-Durmort C, Costet P, Pineau T, Wahli W, Willson TM, and Besnard P (2001). Differential involvement of peroxisome-proliferator-activated receptors alpha and delta in fibrate and fatty-acid-mediated inductions of the gene encoding liver fatty-acid-binding protein in the liver and the small intestine. Biochem. J. 355, 481–488. [PubMed: 11284737]

Poullis A, Foster R, Shetty A, Fagerhol MK, and Mendall MA (2004). Bowel inflammation as measured by fecal calprotectin: a link between lifestyle factors and colorectal cancer risk. Cancer Epidemiol. Biomarkers Prev. 13, 279–284. [PubMed: 14973103]

Puchalska P, and Crawford PA (2017). Multi-dimensional Roles of Ketone Bodies in Fuel Metabolism, Signaling, and Therapeutics. Cell Metab. 25, 262–284. [PubMed: 28178565]

Ringel AE, Drijvers JM, Baker GJ, Catozzi A, García-Cañaveras JC, Gassaway BM, Miller BC, Juneja VR, Nguyen TH, Joshi S, et al. (2020). Obesity Shapes Metabolism in the Tumor Microenvironment to Suppress Anti-Tumor Immunity. Cell 183, 1848–1866.e26. [PubMed: 33301708]

Rodríguez-Colman MJ, Schewe M, Meerlo M, Stigter E, Gerrits J, Pras-Raves M, Sacchetti A, Hornsveld M, Oost KC, Snippert HJ, et al. (2017). Interplay between metabolic identities in the intestinal crypt supports stem cell function. Nature 543, 424–427. [PubMed: 28273069]

Roper J, Tammela T, Cetinbas NM, Akkad A, Roghanian A, Rickelt S, Almeqdadi M, Wu K, Oberli MA, Sánchez-Rivera FJ, et al. (2017). In vivo genome editing and organoid transplantation models of colorectal cancer and metastasis. Nat. Biotechnol. 35, 569–576. [PubMed: 28459449]

Roper J, Tammela T, Akkad A, Almeqdadi M, Santos SB, Jacks T, and Yilmaz ÖH (2018). Colonoscopy-based colorectal cancer modeling in mice with CRISPR-Cas9 genome editing and organoid transplantation. Nat. Protoc 13, 217–234. [PubMed: 29300388]

Sasaki N, Sachs N, Wiebrands K, Ellenbroek SIJ, Fumagalli A, Lyubimova A, Begthel H, van den Born M, van Es JH, Karthaus WR, et al. (2016). Reg4+ deep crypt secretory cells function as epithelial niche for Lgr5+ stem cells in colon. Proc. Natl. Acad. Sci. USA 113, E5399–E5407. [PubMed: 27573849]

Sato T, Vries RG, Snippert HJ, van de Wetering M, Barker N, Stange DE, van Es JH, Abo A, Kujala P, Peters PJ, and Clevers H (2009). Single Lgr5 stem cells build crypt-villus structures in vitro without a mesenchymal niche. Nature 459, 262–265. [PubMed: 19329995]

Sato T, van Es JH, Snippert HJ, Stange DE, Vries RG, van den Born M, Barker N, Shroyer NF, van de Wetering M, and Clevers H (2011). Paneth cells constitute the niche for Lgr5 stem cells in intestinal crypts. Nature 469, 415–418. [PubMed: 21113151]

Schell JC, Wisidagama DR, Bensard C, Zhao H, Wei P, Tanner J, Flores A, Mohlman J, Sorensen LK, Earl CS, et al. (2017). Control of intestinal stem cell function and proliferation by mitochondrial pyruvate metabolism. Nat. Cell Biol. 19, 1027–1036. [PubMed: 28812582]

Schoors S, Bruning U, Missiaen R, Queiroz KCS, Borgers G, Elia I, Zecchin A, Cantelmo AR, Christen S, Goveia J, et al. (2015). Fatty acid carbon is essential for dNTP synthesis in endothelial cells. Nature 520, 192–197. [PubMed: 25830893]

Schulz MD, Atay C, Heringer J, Romrig FK, Schwitalla S, Aydin B, Ziegler PK, Varga J, Reindl W, Pommerenke C, et al. (2014). High-fat-diet-mediated dysbiosis promotes intestinal carcinogenesis independently of obesity. Nature 514, 508–512. [PubMed: 25174708]

Shapira SN, and Christofk HR (2020). Metabolic Regulation of Tissue Stem Cells. Trends Cell Biol. 30, 566–576. [PubMed: 32359707]

Shi Y, Hon M, and Evans RM (2002). The peroxisome proliferator-activated receptor delta, an integrator of transcriptional repression and nuclear receptor signaling. Proc. Natl. Acad. Sci. USA 99, 2613–2618. [PubMed: 11867749]

Shoshkes-Carmel M, Wang YJ, Wangensteen KJ, Tóth B, Kondo A, Massasa EE, Itzkovitz S, and Kaestner KH (2018). Subepithelial telocytes are an important source of Wnts that supports intestinal crypts. Nature 557, 242–246. [PubMed: 29720649]

Smillie CS, Biton M, Ordovas-Montanes J, Sullivan KM, Burgin G, Graham DB, Herbst RH, Rogel N, Slyper M, Waldman J, et al. (2019). Intra-and Inter-cellular Rewiring of the Human Colon during Ulcerative Colitis. Cell 178, 714–730.e22. [PubMed: 31348891]

Soneson C, Love MI, and Robinson MD (2015). Differential analyses for RNA-seq: transcript-level estimates improve gene-level inferences. F1000Res. 4, 1521. [PubMed: 26925227]

Stine RR, Sakers AP, TeSlaa T, Kissig M, Stine ZE, Kwon CW, Cheng L, Lim H-W, Kaestner KH, Rabinowitz JD, and Seale P (2019). PRDM16 Maintains Homeostasis of the Intestinal Epithelium by Controlling Region-Specific Metabolism. Cell Stem Cell 25, 830–845.e8. [PubMed: 31564549]

Stuart T, Butler A, Hoffman P, Hafemeister C, Papalexi E, Mauck WM 3rd, Hao Y, Stoeckius M, Smibert P, and Satija R (2019). Comprehensive Integration of Single-Cell Data. Cell 177, 1888–1902.e21. [PubMed: 31178118]

Subramanian A, Tamayo P, Mootha VK, Mukherjee S, Ebert BL, Gillette MA, Paulovich A, Pomeroy SL, Golub TR, Lander ES, and Mesirov JP (2005). Gene set enrichment analysis: a knowledge-based approach for interpreting genome-wide expression profiles. Proc. Natl. Acad. Sci. USA 102, 15545–15550. [PubMed: 16199517]

Tajan M, and Vousden KH (2020). Dietary Approaches to Cancer Therapy. Cancer Cell 37, 767–785. [PubMed: 32413275]

Wagner N, and Wagner K-D (2020). PPAR Beta/Delta and the Hallmarks of Cancer. Cells 9, 1133.

Wang Y-X, Lee C-H, Tiep S, Yu RT, Ham J, Kang H, and Evans RM (2003). Peroxisome-proliferator-activated receptor delta activates fat metabolism to prevent obesity. Cell 113, 159–170. [PubMed: 12705865]

Wang B, Rong X, Duerr MA, Hermanson DJ, Hedde PN, Wong JS, Vallim T.Q. de A., Cravatt BF, Gratton E, Ford DA, and Tontonoz P (2016). Intestinal Phospholipid Remodeling Is Required for Dietary-Lipid Uptake and Survival on a High-Fat Diet. Cell Metab. 23, 492–504. [PubMed: 26833026]

Wang B, Rong X, Palladino END, Wang J, Fogelman AM, Martín MG, Alrefai WA, Ford DA, and Tontonoz P (2018). Phospholipid Remodeling and Cholesterol Availability Regulate Intestinal Stemness and Tumorigenesis. Cell Stem Cell 22, 206–220.e4. [PubMed: 29395055]

Wang D, Fu L, Wei J, Xiong Y, and DuBois RN (2019). PPARδ Mediates the Effect of Dietary Fat in Promoting Colorectal Cancer Metastasis. Cancer Res. 79, 4480–4490. [PubMed: 31239272]

Xu HE, Stanley TB, Montana VG, Lambert MH, Shearer BG, Cobb JE, McKee DD, Galardi CM, Plunket KD, Nolte RT, et al. (2002). Structural basis for antagonist-mediated recruitment of nuclear co-repressors by PPARalpha. Nature 415, 813–817. [PubMed: 11845213]

Yang K, Yang W, Mariadason J, Velcich A, Lipkin M, and Augenlicht L (2005). Dietary components modify gene expression: implications for carcinogenesis. J. Nutr. 135, 2710–2714. [PubMed: 16251635]

Yilmaz ÖH, Katajisto P, Lamming DW, Gültekin Y, Bauer-Rowe KE, Sengupta S, Birsoy K, Dursun A, Yilmaz VO, Selig M, et al. (2012). mTORC1 in the Paneth cell niche couples intestinal stem-cell function to calorie intake. Nature 486, 490–495. [PubMed: 22722868]

Highlights

- HFD augments intestinal stemness through PPARδ and PPARα
- A PPAR-FAO program enhances stemness and tumorigenicity in a HFD
- Loss or inhibition of Cpt1a-mediated FAO blunts the HFD-enhancing effects in ISCs
- Early intestinal tumors arising from HFD ISCs are highly sensitive to FAO inhibition

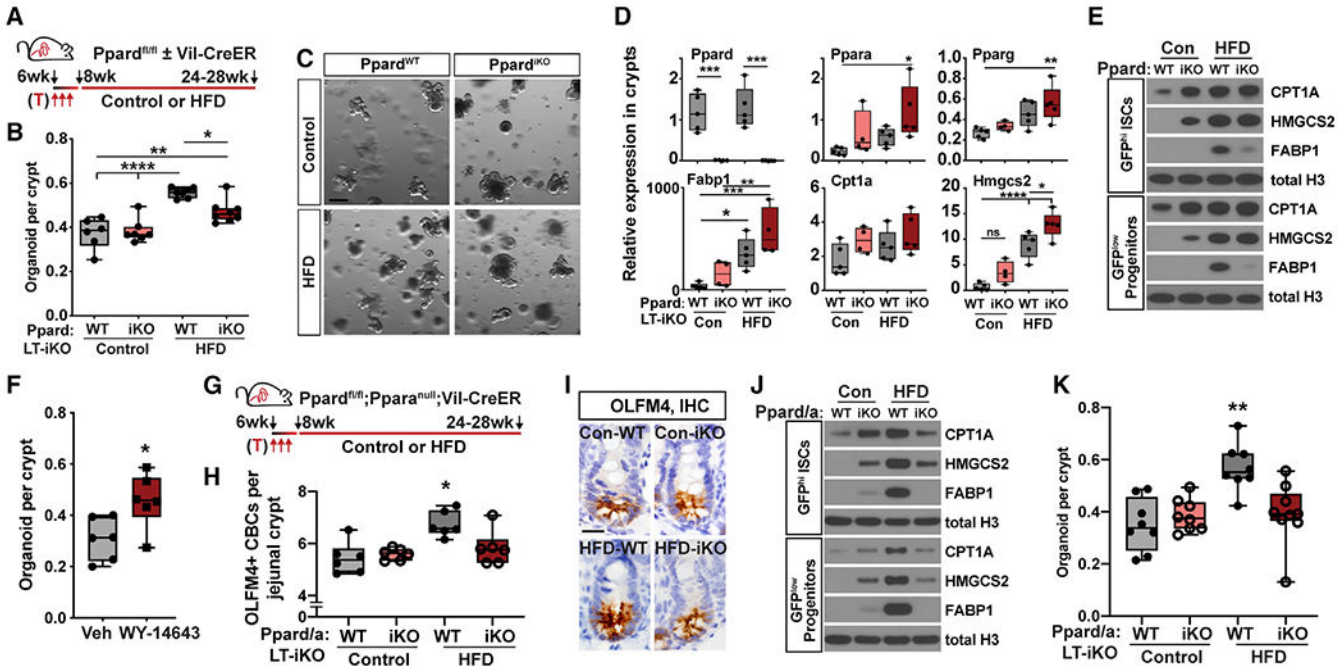

Figure 1. PPARδ and PPARα function redundantly to enhance stem cell activity in a HFD

(A) Schematic of intestinal *Ppard* conditional deletion with *Villin-CreERT2* (*Ppard*-iKO), including timeline of tamoxifen (T) injections for long-term deletion, diet, and tissue collection.

(B and C) Quantification of organoids per crypt from WT (*Ppard*$^{fl/fl}$) or *Ppard*-iKO mice in (A) (B), accompanied by representative bright-field images (C). LT-iKO indicates deletion of intestinal *Ppard* prior to establishment on the diet. Scale bar, 200 μm.

(D) qRT-PCR of transcripts amplified from crypts collected from WT (*Ppard*$^{fl/fl}$) or *Ppard*-iKO mice on chow or HFD. Transcripts were normalized to β-actin.

(E) Immunoblot of flow-sorted ISCs (*Lgr5*-EGFP^{hi}) and progenitors (*Lgr5*-EGFP^{low}) from WT and *Ppard*-iKO (*Ppard*$^{fl/fl}$*; Villin-CreERT2; Lgr5-eGFP-IRES-CreERT2*) mice on a control diet or HFD. *Villin-CreERT2; Lgr5-eGFP-IRES-CreERT2* animals were used as WT controls.

(F) Quantification of organoids per crypt from mice injected daily for 30 days with the PPARα agonist WY-14643 (4 mg/kg) or vehicle.

(G) Schematic of the intestinal *Ppard* conditional allele with *Villin-CreERT2* crossed to *Ppara*-null (*Ppard/a*-iKO), including timeline of T injections, diet, and tissue collection. *Villin-CreERT2* transgenic mice were used as WT controls.

(H) Quantification of OLFM4^{+} cells per jejunal crypt. Each data point represents quantification of 20+ crypts from one animal (n = 6).

(I) Representative images of OLFM4^{+} immunohistochemistry (IHC) from (H). Scale bar, 20 μm.

(J) Immunoblot blot of flow-sorted ISCs (*Lgr5*-EGFP^{hi}) and progenitors (*Lgr5*-EGFP^{low}) from WT and *Ppard/a*-iKO mice on a control diet or HFD. *Ppard/a*-iKO mice carried *Lgr5-eGFP-IRES-CreERT2* for isolation of ISC and progenitor populations. *Villin-CreERT2; Lgr5-eGFP-IRES-CreERT2* animals were used as WT controls.

(K) Quantification of organoids per crypt from mice in (G).

To compare differences in diet, control WT mice were fed chow in (B)–(D) and a purified control diet in (E) and (H)–(K). In (B), (D), (F), and (K), each data point represents the average of 2–3 technical replicates of one animal. *p < 0.05, **p < 0.01, ***p < 0.005, ****p < 0.0001, one-way ANOVA.

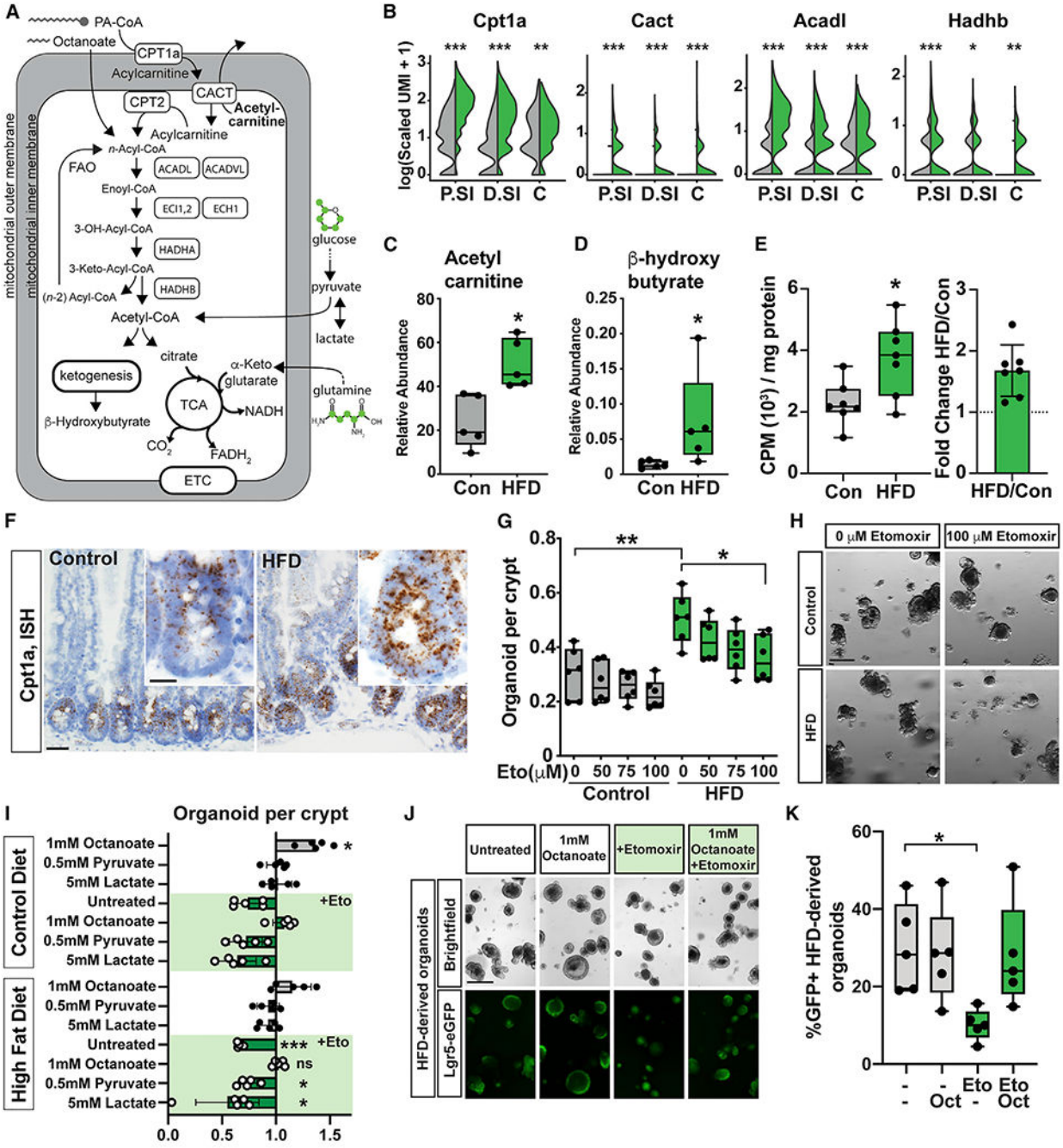

Figure 2. HFD fuels FAO in ISCs

(A) Schematic of mitochondrial FAO involving key processes, proteins, metabolites, and fuel inputs.

(B) Log(UMIs per 10K + 1) expression of genes integral to the FAO in ISCs from control-fed (gray, n = 2) or HFD-fed mice (green, n = 3) (P.SI, proximal small intestine; D.SI, distal small intestine; C, colon). Benjamini-Hochberg-corrected p values: *$p < 10^{-2}$, **$p < 10^{-5}$, ***$p < 10^{-10}$.

(C and D) Relative abundance of the FAO-mediated metabolites acetylcarnitine (C) and BOHB (D) isolated from freshly harvested crypts and measured by liquid chromatography-mass spectrometry (LC-MS).

(E) FAO activity (counts per minute [cpm]) of metabolized ^{3}H-palmitic acid normalized to total protein in crypts from control and HFD-fed mice, accompanied by the fold change calculated as the ratio of HFD cpm per control cpm.

(F) Single-molecule RNA *in situ* hybridization (ISH) of *Cpt1a* in WT tissue from control and HFD-fed mice. Scale bars, 50 μm and 20 μm (inset).

(G and H) Quantification of organoids per crypt from control or HFD-fed mice grown in culture (ADMEM medium) with increasing concentrations of the irreversible CPT1A inhibitor etomoxir (Eto) (G), accompanied by representative images (H). Scale bar, 200 μm.

(I) Quantification of organoids per crypt from control or HFD-fed mice, grown in RPMI 1640 basal medium with or without Eto (37.5 μM) and supplemented with octanoate (1 mM), sodium pyruvate (0.5 mM), or sodium-L-lactate (5 mM).

(J) Representative images of HFD-derived *Lgr5*-EGFP^{+} organoids in (I). Scale bar, 200 μm.

(K) Quantification of HFD-derived *Lgr5*-eGFP^{+} organoids grown in the presence of octanoate (1 mM) or Eto (37.5 μM).

In (B)–(I), mice were fed a purified control diet or HFD. In (E), (G), and (I), each data point represents the average of 3+ technical replicates from one animal. *$p < 0.05$, **$p < 0.01$, ***$p < 0.005$; ns, not significant; one-way ANOVA.

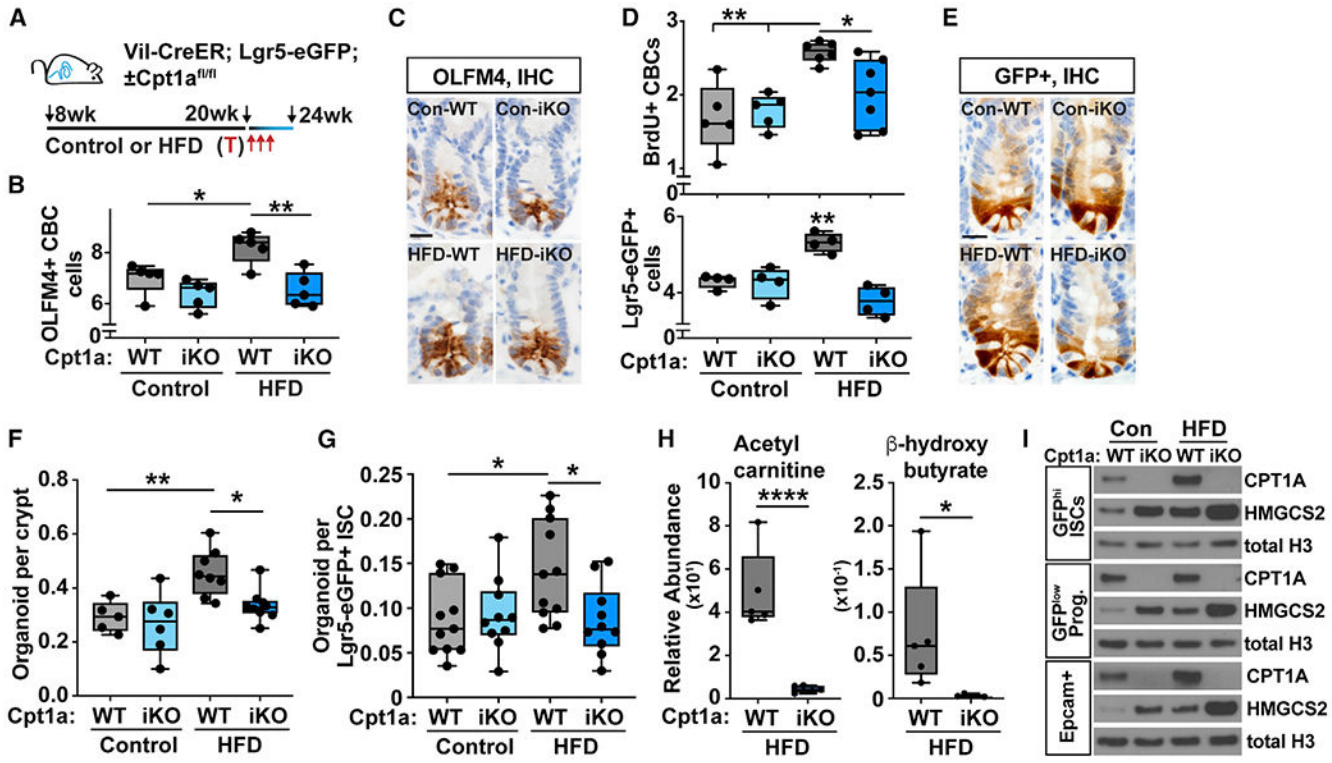

Figure 3. CPT1A-mediated FAO promotes HFD ISC stemness

(A) Schematic of intestinal *Cpt1a* conditional deletion with *Villin-CreERT2; Lgr5-eGFP-IRES-CreERT2* (*Cpt1a*-iKO), including timeline of T injections, diet, and tissue collection. *Villin-CreERT2; Lgr5-eGFP-IRES-CreERT2* animals were used as controls.

(B and C) Quantification of OLFM4^{+} cells per jejunal crypt (B) with representative images (C). Scale bar, 20 μm.

(D and E) Quantification of BrdU^{+} and EGFP^{+} CBC cells per jejunal crypt (D) with representative images (E). Scale bar, 20 μm.

(F and G) Quantification of organoid per crypt (F) or *Lgr5*-EGFP^{hi} ISC (G) from control or HFD-fed mice carrying WT or deleted copies of *Cpt1a* (iKO).

(H) Relative abundance of the FAO-mediated metabolites acetylcarnitine and BOHB isolated from freshly harvested crypts of HFD-fed mice and measured by LC-MS.

(I) Immunoblot blot of flow-sorted ISCs (*Lgr5*-EGFP^{hi}), progenitors (*Lgr5*-EGFP^{low}), and epithelial crypt (EpCAM^{+}) cells from WT and *Cpt1a*-iKO mice on a control diet or HFD.

(B)–(E) were reprinted from Beyaz et al. (2021). In (A)–(I), mice were fed a purified control diet or HFD. In (F) and (G), each data point represents the average of 3+ technical replicates from one animal. *p < 0.05, **p < 0.01, ***p < 0.005, ****p < 0.0001, one-way ANOVA.

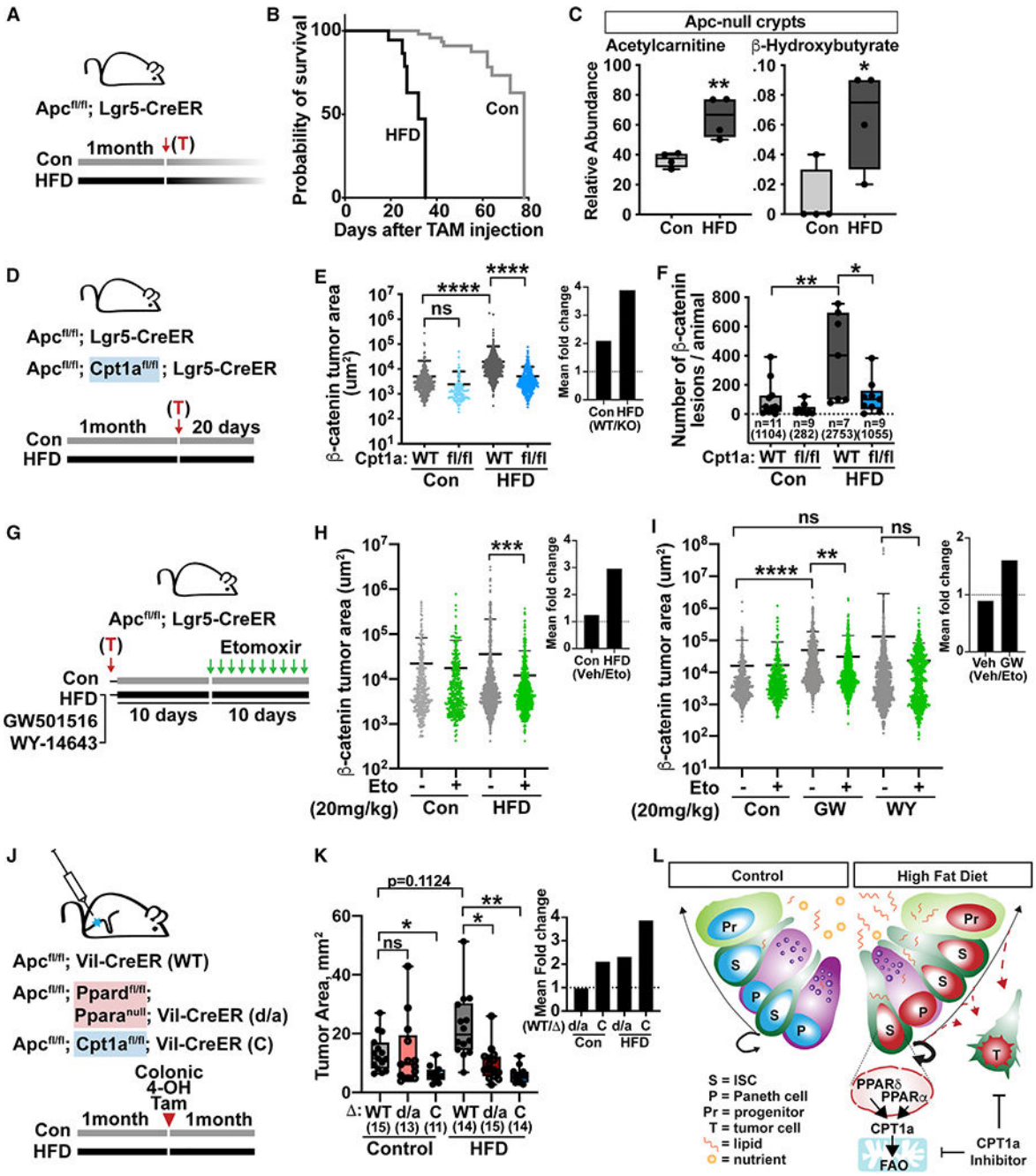

Figure 4. HFD-initiated tumors are metabolically vulnerable to FAO disruption

(A) Schematic of the Apc tumor model with *Lgr5-eGFP-IRES-CreERT2* driving *Apc*$^{fl/fl}$ excision specifically in *Lgr5-CreERT2* stem cells upon T induction (25 mg/kg) 1 month after establishment on a control diet or HFD.

(B) Kaplan-Meier survival curve of the mice in (A).

(C) Relative abundance of the FAO-mediated metabolites acetylcarnitine and BOHB isolated from freshly harvested crypts of *Apc*$^{fl/fl}$*; Villin-CreERT2* mice and measured by LC-MS.

(D) Schematic of *Apc*$^{fl/fl}$*; Lgr5-eGFP-IRES-CreERT2* tumor initiation model with or without the *Cpt1a*$^{fl/fl}$ allele. Mice were put on a control diet or HFD for 1 month prior to a single T injection (25 mg/kg), followed by 20 days before tissue collection.
(E and F) Quantification of the area (E) and number (F) of β-catenin^{+} adenomas in the proximal half of the intestine.
(G-I) Schematic of Apc$^{fl/fl}$; *Lgr5-eGFP-IRES-CreERT2* tumor progression model (G). Mice receive a single T injection (25 mg/kg) to induce adenoma formation. The following day, cohorts are established on a control diet or HFD (H) or treated with daily injections of vehicle, GW501516 (GW; 4 mg/kg), or WY-14643 (WY; 4 mg/kg) (I). The diet regimen or agonist administration was extended for 20 days. On days 11–20 before tissue collection, mice received daily injections of the CPT1A inhibitor Eto (20 mg/kg). Shown is quantification of the β-catenin^{+} tumor area in mice under HFD conditions (H) and GW or WY administration (I) according to the regimens in (G). The inset plots represent the mean area fold change between non-Eto and +Eto recipients of a given treatment.
(J) Schematic of endoscopy-guided colonic injections with 4-OH Tamoxifen (Tam) 1 month after start of the control diet or HFD.
(K) Quantification of tumor area 1 month after injection. The mean fold change of WT versus mutant is depicted in the right graph inset.
(L) Model of ISC adaptation to a HFD: PPARδ and PPARα instruct a transcriptional program in response to a HFD that promotes CPT1A-mediated FAO. In contrast to a control diet, genetic loss or inhibition of *Cpt1a* on a HFD disrupts tumor initiation and progression. Control mice were fed chow in (B) and (I) and a purified control diet in (C), (E), (F), (H), and (K). *$p < 0.05$, **$p < 0.01$, ***$p < 0.005$, ****$p < 0.0001$, one-way ANOVA.

KEY RESOURCES TABLE

REAGENT or RESOURCE	SOURCE	IDENTIFIER
Antibodies		
Mouse Cpt1a	Abcam	Cat#: ab128568; RRID: AB_11141632
Rabbit Hmgcs2	Abcam	Cat#: ab137043; RRID: AB_2749817
Rabbit Fabp1	Cell Signaling Technology	Cat#: 13368S; RRID: AB_2798192
Rabbit Pdk4	Abcam	Cat#: ab214938; RRID: AB_2864318
Rabbit H3	Cell Signaling Technologies	Cat#: 4499S; RRID: AB_10544537
Rabbit γ-tubulin	Sigma Aldrich	Cat#: T5198
Rabbit Olfm4	Cell Signaling Technologies	Cat#: 39141S; RRID: AB_2650511
Rabbit GFP	Cell Signaling Technologies	Cat#: 2956S; RRID: AB_1196615
Mouse β-catenin	BD Biosciences	Cat#: 610154; RRID: AB_397555
Rat BrdU	Abcam	Cat#: ab6326; RRID: AB_305426
Rabbit Lysozyme	Thermo Fisher	Cat#: RB-372-A1; RRID: AB_138387
Rabbit ChromograninA	Abcam	Cat#: ab15160; RRID: AB_301704
Rabbit Ki67	Abcam	Cat#: ab15580; RRID: AB_443209
Rabbit β-catenin	Abcam	Cat#: ab32572; RRID: AB_32572
Rabbit Cleaved Caspase 3	Cell Signaling Technologies	Cat#: 9664S; RRID: AB_2070042
Rabbit phospho-histone H2A.X	Cell Signaling Technologies	Cat#: 2577S; RRID: AB_2118010
CD45-PE, clone 30-F11	eBioscience	Cat#: 12-0451-83; RRID: AB_465669
CD31-PE, clone Mec 13.3	Biolegend	Cat#: 102514; RRID: AB_102514
Ter-119-PE	Biolegend	Cat#: 116208; RRID: AB_313709
CD24-Pacfic Blue, clone M1/69	Biolegend	Cat#: 101820; RRID: AB_572011
CD117-APC/Cy7, clone 2B8	Biolegend	Cat#: 105826; RRID: AB_1626278
EpCAM APC, clone G8.8	eBioscience	Cat#: 17-5791-82; RRID: AB_2716944
Chemicals, peptides, and recombinant proteins		
GW501516	Sigma Aldrich	Cat#: SML1491
PEG400	Sigma Aldrich	Cat#: P4338
Tween-80	Sigma Aldrich	Cat#: P4780
GW6471	Tocris	Cat#: 4618
WY14643	Sigma Aldrich	Cat#: C7801
Tamoxifen	Sigma Aldrich	Cat#: T5648-1G
Sunflower Seed Oil	Spectrum	Cat#: S1929
5-Bromo-2′-deoxyuridine	Sigma Aldrich	Cat#: 19-160
Matrigel	Corning	Cat#: 356231
Advanced DMEM	GIBCO	Cat#: 12491015
EGF	Peprotech	Cat#: 315-09
Noggin	Peprotech	Cat#: 250-38
R-spondin	Peprotech	Cat#: 315-32

REAGENT or RESOURCE	SOURCE	IDENTIFIER
N-acetyl-l-cystine	Sigma Aldrich	Cat#: A9165
B27	Life Technologies	Cat#: 17504044
Chir99021	LC Laboratories	Cat#: C-6556
Y-27632 dihydrochloride	Sigma Aldrich	Cat#: Y0503
48 well plates	Olympus	Cat#: 25-108
96 well plates	Olympus	Cat#: 25-109
Etomoxir	Sigma Aldrich	Cat#: E1905
Sodium octanoate	Sigma Aldrich	Cat#: C5038
Sodium pyruvate	Sigma Aldrich	Cat#: P8574
Sodium-L-lactate	Sigma Aldrich	Cat#: L7022
D-(+)-glucose	Sigma Aldrich	Cat#: G7021
JAG-1	Anaspec	Cat#: AS-61298
TRI Reagent	Sigma Aldrich	Cat#: 93289
qScript cDNA SuperMix	Quantabio	Cat#: 95048
PerfeCTa SYBR green fast mix	Quantabio	Cat#: 95072
WesternBright Sirus	Advasta	Cat#: K12043D20
Elite ABC HRP Kit	Vector Laboratories	Cat#: PK6100
Signalstain® DAB Substrate Kit	Cell Signaling Technologies	Cat#: 8049S
Signalstain® Antibody Diluent	Cell Signaling Technologies	Cat#: 8112L
7AAD	Invitrogen	Cat#: A1310
RMPI (− glucose, + glutamine)	GIBCO	Cat#: 11879020
Prolong Gold Antifade Mountant with DAPI	Invitrogen	Cat#: P36941
D-Glucose (U13C6, 99%)	Cambridge Isotope Laboratories	Cat#: CLM-1396-PK
L-Glutamine (U13C5, 99%)	Cambridge Isotope Laboratories	Cat#: CLM-1822H-PK
Palmitic Acid [9,10-3H(N)]-1mCi (37 MBq)	Perkin Elmer	Cat#: NET043001MC
Bovine Serum Albumin	Sigma Aldrich	Cat#: A6003
Dowex 1x8 chloride resin	Sigma Aldrich	Cat#: 217425
EcoLume	MP Biomedicals	Cat#: 882470
(Z)-4-hydroxytamoxifen	Calbiochem	Cat#: 579002
Deposited data		
RNA sequencing Data	GEO repository	GSE151047
RNA sequencing Data	GEO repository	GSE164832
Experimental models: Organisms/strains		
$Cpt1a^{fl/fl}$	Dr. Peter Carmeliet	Schoors et al., 2015
Villin-CreERT2	Dr. Sylvie Robine, The Jackson Laboratory	Stock No: 020282
Lgr5-eGFP-IRES-CreERT2	The Jackson Laboratory	Stock No: 008875
$Rosa26\text{-}LSL\text{-}LacZ^{fl/fl}$	The Jackson Laboratory	Stock No: 003474
$Apc^{fl/fl}$ (exon14)	Dr. Christine Perret	Colnot et al., 2004

REAGENT or RESOURCE	SOURCE	IDENTIFIER
Ppard$^{fl/fl}$	The Jackson Laboratory	Stock No: 005897
Ppara$^{-/-}$	The Jackson Laboratory	Stock No: 003580
Ppard$^{fl/fl}$; Villin-CreERT2	Yilmaz Lab	Beyaz et al., 2016
Ppard$^{fl/fl}$; Villin-CreERT2; Lgr5-eGFP-IR ES-CreERT2	First presented in this work	N/A
Ppard$^{fl/fl}$; Ppara$^{-/-}$; Villin-CreERT2; Lgr 5-eGFP-IRES-CreERT2	First presented in this work	N/A
Ppara$^{-/-}$; Villin-CreERT2; Lgr5-eG FP-IRES-CreERT2	First presented in this work	N/A
Ppard$^{fl/fl}$; Ppara$^{-/-}$; Lgr5-eGFP-IRES-CreERT2; Rosa26-LSL-LacZ$^{fl/fl}$	First presented in this work	N/A
Ppard$^{fl/fl}$; Ppara$^{-/-}$; Villin-CreERT2	First presented in this work	N/A
Cpt1a$^{fl/fl}$; Villin-CreERT2; Lgr5-GFP-IR ES-CreER	First presented in this work	N/A
Cpt1a$^{fl/fl}$; Lgr5-eEGFP-IRES-CreERT2; Rosa26-LSL- LacZ$^{fl/fl}$	First presented in this work	N/A
Apc$^{fl/fl}$; Lgr5-eGFP-IRES-CreERT2; Rosa26-LSL-LacZ$^{fl/fl}$	Yilmaz Lab	Beyaz et al., 2016
Cpt1a$^{fl/fl}$; Apc$^{fl/fl}$; Lgr5-eGFP-IRES-CreERT2	First presented in this work	N/A
Apc$^{fl/+}$; Lgr5-eGFP-IRES-CreERT2; Rosa26-LSL-LacZ$^{fl/fl}$	First presented in this work	N/A
Apc$^{fl/+}$; Cpt1a$^{fl/fl}$; Lgr5-eGFP-IRES-CreERT2; Rosa26-LSL-LacZ$^{fl/fl}$	First presented in this work	N/A
Ppard$^{fl/fl}$; Ppara$^{-/-}$; Apc$^{fl/fl}$; Villin-CreERT2	First presented in this work	N/A
Cpt1a$^{fl/fl}$; Apc$^{fl/fl}$; Villin-CreERT2	First presented in this work	N/A
Apc$^{fl/fl}$; Villin-CreERT2	Yilmaz Lab	Roper et al., 2017
Oligonucleotides		
See Table S1 for rt-PCR primers	Integrated DNA Technologies (IDT)	N/A
Software and algorithms		
FlowJo v10	FlowJo LLC.	https://www.flowjo.com/
GraphPad Prism 8	GraphPad Software	https://www.graphpad.com/scientific-software/prism/
ImageJ-Fiji	National Institutes of Health, USA	https://fiji.sc/
Qlucore Omics Explorer 3.2	Qlucore	https://www.qlucore.com/
Tracefinder 4.1	Thermo Scientific	https://www.thermofisher.com/us/en/home.html
Other		
Standard Chow	LabDiet	Ref#: 5P76
High-Fat Diet	Research Diets	Ref#: D12492
Control Diet	Research Diets	Ref#: D12450J
In situ hybridization probe for mouse Cpt1a: Mm-Cpt1a	Advanced Cell Diagnostics	Probe No: 443071
In situ hybridization probe for mouse Ppara: Mm-Ppara	Advanced Cell Diagnostics	Probe No: 454051